Biological Aging of CNS-Resident Cells Alters the Clinical Course and Immunopathology of Autoimmune Demyelinating Disease

Jeffrey R. Atkinson[1,2], Andrew D. Jerome[1,2], Andrew R. Sas[1,2], Ashley Munie[1,2,3], Cankun Wang[4], Anjun Ma[4], W. David Arnold[1,2], and Benjamin M. Segal[1,2]

[1]Department of Neurology, College of Medicine, The Ohio State University Wexner Medical Center, Columbus, OH, USA.
[2]The Neuroscience Research Institute, The Ohio State University, Columbus, OH, USA.
[3]Graduate Program in Immunology, University of Michigan Medical School, Ann Arbor, MI, USA
[4]Department of Biomedical Informatics, College of Medicine, The Ohio State University, Columbus, OH, USA

Corresponding Author: Segal, BM
Email: Benjamin.segal@osumc.edu

Abstract

Biological aging is the strongest factor associated with the clinical phenotype of multiple sclerosis (MS). Relapsing remitting MS (RRMS) typically presents in the third or fourth decade, while the mean age of presentation of progressive MS (pMS) is 45 years old. Here we show that experimental autoimmune encephalomyelitis (EAE), induced by the adoptive transfer of encephalitogenic $CD4^+$ Th17 cells, is more severe, and less like to remit, in middle-aged compared with young adult mice. Donor T cells and neutrophils are more abundant, while B cells are relatively sparse, in central nervous system (CNS) infiltrates of the older mice. Experiments with reciprocal bone marrow chimeras demonstrate that radio-resistant, non-hematopoietic cells play a dominant role in shaping age-dependent features of the neuroinflammatory response, as well as the clinical course, during EAE. Reminiscent of pMS, EAE in middle-aged adoptive transfer recipients is characterized by widespread microglial activation. Microglia from older mice express a distinctive transcriptomic profile, suggestive of enhanced chemokine synthesis and antigen presentation. Collectively, our findings suggest that drugs that suppress microglial activation, and acquisition or expression of aging-associated properties, may be beneficial in the treatment of progressive forms of inflammatory demyelinating disease.

34 ## Introduction

35 Traditionally, people with multiple sclerosis (MS) are categorized into 2 major clinical subsets based on
36 whether they experience a relapsing-remitting or progressive course. Relapsing-remitting MS (RRMS)
37 is characterized by discrete, self-limited episodes of neurological signs and symptoms that persist for
38 weeks to months, followed by a partial or full recovery. Clinical relapses are associated with the
39 appearance of acute inflammatory demyelinating lesions in central nervous system (CNS) white matter,
40 which are driven by the infiltration of lymphocytes and myeloid cells from the blood stream into the CNS
41 across leaky cerebrovascular venules (1). In contrast, progressive MS (pMS) involves an insidious,
42 gradual decline in neurological function (most often in the form of worsening paraparesis, gait
43 imbalance, and/or dementia), in the absence of focal blood-brain-barrier (BBB) breakdown or the influx
44 of peripheral immune cells. Typical pathological features of pMS include slowly expanding white matter
45 lesions, composed of a gliotic core surrounded by a rim of activated microglia, as well as widespread
46 microglia activation in the macroscopically normal appearing white matter (1, 2). Disease modifying
47 therapies (DMT) that are approved for the treatment of MS mostly target lymphocytes in the peripheral
48 immune system. While highly efficacious in RRMS, they have a modest therapeutic impact, at best, in
49 pMS. There is an unmet need for new treatments that slow, or even block, the accumulation of disability
50 in individuals with pMS. The identification of novel therapeutic targets pertinent to pMS will require a
51 deeper understanding of the pathogenic effector cells, mediators, and pathways specific to the
52 manifestation of progressive disease.

53 Biological aging is the strongest factor associated with MS clinical phenotype. RRMS typically
54 presents in the third or fourth decade, while the mean age of onset of pMS is 45 years old (3). The age
55 of onset of pMS is similar whether it occurs at clinical presentation (referred to as primary progressive
56 MS or PPMS), or follows an initial RR phase (secondary progressive MS or SPMS). Progressive MS is
57 rare before age 40, and virtually non-existent in the pediatric population (4). MS relapse rates tend to
58 decline with disease duration and chronological age (5). Collectively, these data suggest that

59 physiological changes associated with biological aging interact with the autoimmune response that
60 drives CNS damage during MS, in a manner that transforms the clinical course and underlying
61 neuropathology to a progressive pattern. Biological aging could impact the pathogenesis of MS via
62 direct effects on immune cells or CNS-resident cells. Regarding the former, aging leads to
63 immunosenescence, including a chronic, low-grade inflammatory state referred to as “inflamm-aging”.
64 Regarding the latter, aging CNS tissues may be more vulnerable to inflammatory insults and less
65 capable of initiating repair. The relative contributions of these aging-related phenomena to chronic
66 active lesions, widespread microglial activation, and relentless accumulation of disability during pMS
67 remains to be elucidated.

68 Experimental autoimmune encephalomyelitis (EAE), the most popular animal model of MS,
69 generally presents with an acute monophasic or RR course (6). The pathological features of EAE, such
70 as multifocal BBB breakdown and CNS influx of hematogenous leukocytes, are more reminiscent of
71 RRMS than pMS. EAE is traditionally induced in young adult mice, between 8-12 weeks of age (7).
72 There is a dearth of studies examining the impact of biological aging on animal models of inflammatory
73 demyelination. Here we compare the clinical course, neuropathology, and inflammatory milieu of EAE
74 in young adult versus middle-aged mice.

75

76 Results

77 *Biological aging exacerbates the effector phase of EAE*.

78 In order to distinguish between the effect of biological aging during the T cell-priming and
79 effector stages of EAE, we employed an adoptive transfer model in which IL-23-polarized MOG_{35-55}-
80 reactive $CD4^+$ T cells from donors of different ages are injected into naïve syngeneic recipients of
81 different ages. Traditionally, EAE is induced in young adult mice, between 8 to 12 weeks of age. For

82 the middle-aged cohort, we used mice 40-44 weeks of age, based on their general developmental
83 similarity to humans at the mean age of onset for pMS (8). We found no significant differences in the
84 clinical course of EAE induced by encephalitogenic $CD4^+$ T cells derived from MOG-immunized young
85 adult versus middle-aged donors (Supplementary Figure 1). In contrast, the clinical course of EAE was
86 accelerated and exacerbated in middle-aged, compared with young adult, adoptive transfer recipients
87 that had been injected with the same pool of encephalitogenic $CD4^+$ T cells (Fig. 1). Middle-aged
88 recipients developed neurological deficits earlier, had higher peak scores, and more cumulative
89 neurological disability (Fig. 1 A-C). Middle-aged recipients exhibited greater weight loss, and a
90 significant proportion succumbed to disease (58%), while all of the young recipients survived (Fig.1 D,
91 E). Moreover, approximately 80% of young adult recipients underwent clinical remission, compared with
92 approximately 40% of their middle-aged counterparts (Fig. 1 F). This divergence in clinical courses
93 between the 2 groups was reflected in pathological findings. Immunohistochemical analysis of spinal
94 cord sections revealed more extensive demyelination, associated with parenchymal infiltration by
95 $CD45^{hi}$ hematogenous leukocytes, in the middle-aged cohort (Fig. 2). Electrophysiological studies were
96 performed to assess the functional integrity of the spinal cord. Motor-evoked responses following
97 cervical spinal cord stimulation showed delayed responses in all mice at peak and chronic stages of
98 EAE compared with baseline, indicative of demyelination in the corticospinal tracts (Fig. 3B). By week 2
99 post-transfer, the delay in nerve signal propagation was significantly longer in middle-aged hosts (Fig.
100 3C), consistent with enhanced myelin damage, as had also been revealed by immunohistochemistry. In
101 addition, from day 13 post-transfer onward, middle-aged mice exhibited a greater reduction in motor-
102 evoked potential amplitudes compared with young adult mice, signifying increased axonal dysfunction
103 and/or loss (Fig. 3D). Motor unit number estimation (MUNE) is calculated by dividing the maximum
104 compound muscle action potential amplitude, obtained with sciatic nerve stimulation, by the average
105 single motor unit potential. MUNE, which reflects the number of motor units innervating single muscles,
106 was lower in the sciatic innervated hindlimb muscles of middle-aged hosts on day 27 post-transfer (Fig.
107 3E), consistent with a greater loss or dysfunction of motor neurons in the lumbar spinal cord.

108 *Encephalitogenic T cells and neutrophils are expanded, while B cells are retracted, in CNS infiltrates of*
109 *middle-aged mice with EAE*.

110 The exacerbated clinical course of EAE in older mice could be secondary to a more virulent
111 neuroimmune response, increased susceptibility of CNS-resident cells/myelin to immune-mediated
112 damage, or a combination of these mechanisms. To investigate the former possibility, we compared the
113 cellular composition of neuroinflammatory infiltrates between middle-aged and young adult mice on day
114 10 post-T cell transfer. There were significantly higher frequencies of $CD4^+$ T cells and neutrophils, and
115 a lower frequency of B cells, among $CD45^+$ cells isolated from the spinal cords of the middle-aged
116 recipients (Fig. 4A-C). There were no differences between groups in the frequencies of macrophage/
117 monocytes or monocyte-derived dendritic cells (Supplementary Figure 2). For our experiments, we
118 routinely obtain MOG_{35-55}-primed $CD4^+$ T cells from $CD45.1^+$ congenic donors, in order to distinguish
119 the transferred encephalitogenic T cells from $CD45.2^+$ bystander host T cells. We found that $CD45.1^+$
120 $CD4^+$ T cells were disproportionately expanded in the CNS of middle-aged recipients (Fig. 4B). A broad
121 panel of pro-inflammatory and chemotactic factors were up-regulated in spinal cord lysates of all mice
122 with EAE, but were consistently elevated to higher levels in older mice. These factors include the
123 chemokines CCL5, CXCL9 and CXCL10, which have been shown to target encephalitogenic T cells (9,
124 10), and CXCL1 and CXCL2, the major chemoattractants of mature neutrophils (11, 12) (Fig. 5).
125 Neutrophil-mobilizing factors GM-CSF and G-CSF were also expressed at higher levels in spinal cord
126 lysates obtained from older mice.

127

128 *GM-CSF promotes the early, but not late, stage of exacerbated EAE in aged mice.*

129 We have previously shown that GM-CSF receptor (GM-CSFR)-deficient mice are relatively
130 resistant to adoptively transferred EAE (13). They experience a milder course than wild-type
131 counterparts, with an increased rate of remission. In addition, GM-CSFR deficiency is associated with a
132 lower percent of $CD4^+$ donor T cells and neutrophils, and a higher percent of B cells, in CNS infiltrates,
133 which is the mirror image of the pattern that we observed in middle-age, wild-type mice with EAE.

134 Collectively, these observations suggest that the exacerbated form of EAE that occurs in middle-aged
135 wild-type mice is GM-CSF-driven. Indeed, the absolute number of GM-CSF-expressing donor $CD4^+$ T
136 cells in CNS infiltrates, the level of intracellular GM-CSF in CNS donor T cells, and the level of GM-CSF
137 protein in CNS lysates, were higher in the older versus younger mice with EAE (Fig. 5, Fig.6A, B).
138 Furthermore, single-cell RNA sequencing revealed heightened expression of transcripts encoding GM-
139 CSF, as well as IL-17 and other pro-inflammatory factors, in $CD4^+$ T cells isolated from the CNS of
140 middle-aged mice on day 6 post-transfer, when compared with their younger counterparts (Fig. 6C).
141 Treatment of middle-aged hosts with a neutralizing antibody against GM-CSF, beginning from the day
142 of transfer onward, delayed clinical onset and ameliorated the early clinical course (Fig. 6D, E).
143 However, mean peak scores, cumulative chronic disability, and mortality rates were similar between the
144 anti-GM-CSF and control antibody treatment groups (Fig. 6D, F, and data not shown). Postponing the
145 initiation of anti-GM-CSF treatment to the time of peak disease had no therapeutic impact (data not
146 shown). Based on these data, we concluded that GM-CSF promotes aggressive EAE in older recipients
147 in the early phase of disease, but becomes dispensable as the disease progresses towards a more
148 chronic phase.
149
150 *Radio-resistant, non-hematopoietic cells shape the neuroinflammatory infiltrate and drive exacerbated*
151 *EAE in middle-aged mice.*
152 Next, we sought to determine whether the increased susceptibility of older mice to EAE is
153 secondary to the biological aging of radio-sensitive, hematopoietic cells (that are recruited from the
154 circulation to the CNS) and/or radio-resistant, non-hematopoietic cells (including CNS-resident cells).
155 To that end, we constructed reciprocal bone marrow (BM) chimeric mice with young adult or middle-
156 aged BM cell donors and/or irradiated hosts (Fig. 7A). Middle-aged → middle-aged and young adult →
157 young adult chimeras served as controls. EAE was induced in all immune reconstituted chimeric mice
158 via the adoptive transfer of the same pool of MOG_{35-55} encephalitogenic $CD4^+$ T cells. Irrespective of the
159 age of the BM cell donors, middle -aged BM cell hosts experienced a severe clinical course of EAE,

160 with high mortality rates, while young adult BM cell hosts experienced a milder course with relatively
161 low mortality rates (Fig. 7 B, C). Furthermore, the cellular composition of neuroinflammatory infiltrates in
162 chimeras correlated with the age of the BM cell host, but not the donor, mouse. Middle-aged BM cell
163 hosts reconstituted with young BM cells contained higher frequencies of $CD4^+$ T cells in EAE lesions
164 compared with chimeras that were constructed using young adult hosts, mimicking the results we
165 obtained with non-chimeric mice (Fig. 7D, left panel). Furthermore, the frequency of B cells tended to
166 be lower, while that of neutrophils tended to be higher, in CNS infiltrates of the middle-aged hosts,
167 though not reaching statistical significance (Fig. 7D, middle and right panels). Hence, the age of radio-
168 resistant, non-hematopoietic cells is a dominant factor in determining the phenotype and severity of
169 EAE.
170
171 *Aged microglia exhibit distinct transcriptomes and phenotypes during homeostasis, as well as EAE.*
172 Our finding that radio-resistant cells influence the make-up of neuroinflammatory infiltrates
173 directed our attention towards the role of microglia. In addition to their potential to serve as antigen-
174 presenting cells, microglia produce chemotactic and pro-inflammatory molecules that could orchestrate
175 the recruitment, positioning, and polarization of leukocyte subsets in EAE lesions. A growing body of
176 data indicates that microglia become spontaneously activated and acquire pro-inflammatory signatures
177 with age (14, 15). In support of these published studies, we found that a significant percent of microglia
178 in naïve middle-aged, but not young adult, mice exhibit enhanced expression of the cell surface marker
179 CD11c (Fig. 8A). Bulk RNA sequencing studies showed that microglia isolated from unmanipulated
180 middle-aged mice express elevated levels of pro-inflammatory genes (Fig. 8B, left upper panel), and
181 lower levels of homeostatic genes (Fig. 8B, left lower panel), compared with microglia from their
182 younger counterparts. Furthermore, a number of genes that were disproportionately up-regulated in the
183 middle-aged microglia (such as S*pp1,* C*xcl10*, *Ccl3*, *Il1β, Ccl4*, and *Tnf*) overlapped with previously
184 published transcriptomes of aging microglial subsets enriched in geriatric mice (Fig. 8B, right) (14).

185 Next, we performed single-cell RNA sequencing (scRNA-seq) of CNS CD45$^+$ mononuclear cells
186 isolated from young adult and middle-aged mice during peak EAE. The raw scRNA-seq expression
187 matrix contains 38,057 cells (including 19,899 cells from middle-aged mice and 18,158 cells from young
188 adult) and 19,449 genes. The microglial cells fell into 2 clusters (Fig. 9A). Cluster 1 microglia from
189 middle-aged mice are enriched in transcripts associated with antigen-processing and presentation
190 (including *H2-Aa, H2-Ab1, H2-D1, H-2-Eb1, H2K1, H-2Q7, B2m, Cd74*), and proteasome assembly and
191 function (*Psmb4, Psmb8, Psmb9, Psmb10, Psme1, Psme2*), as well as transcripts that encode pro-
192 inflammatory molecules (*Tnf*, *Il1a*, *Il1b*, *Il18*) (Fig. 9 B, C and Fig. 10A), when compared with their
193 counterparts from young adoptive transfer recipients. In contrast, they are relatively deficient in
194 transcripts associated with homeostasis (*Tmem119*, *Fcrls, Cx3cr1, P2ry12*) and heat shock protein
195 responses *(Dnaja1, Dnajb1, Hspa1a*, *Hspa1b*, *Hspa5*, *Hsp90aa1*, *Hsp90ab1*) (Fig. 9 B, C and
196 Fig.10A). Cluster 2 microglia from middle-aged mice express relatively high levels of genes encoding
197 chemotactic factors (including *Ccl4, Cxcl2, Cxcl9,* and *Cxcl10*) and relatively low levels of genes
198 associated with homeostasis (including *Fcrls*, *Tmem119*, *P2ry12*, and *Cx3cr1*) (Fig. 10 B). Middle-aged
199 microglia in both clusters expressed relatively high expression levels of interferon responses genes
200 (including *Gbp2*, *Ifitm3*, I*fi27l2a*, *Isg15)* (Fig. 10 A, B), as well as genes that are expressed at high
201 levels in microglia located at the rims of slow expanding lesions in people with pMS (*C1qa*, *C1qb*,
202 *C1qc*, *Cstb*, *Fth1*, *Ftl1*, and a panel of ribosomal proteins) (Supplementary Fig. 3).
203

204 ## Discussion

205 Progressive MS typically presents during middle age, whether or not it is preceded by a RR course. It
206 rarely, if ever, occurs in the pediatric MS population (4). Progressive MS has distinctive pathological
207 features that are not characteristic of RRMS in younger individuals, including widespread microglial
208 activation (1). These observations indicate that biological aging has a profound influence on the
209 evolution and manifestation of autoimmune neuroinflammation, but the underlying mechanisms are

210 poorly understood. Here we show that EAE, induced by the transfer of a common pool of IL-23-
211 polarized, MOG-reactive $CD4^+$ T cells, is more severe, and less likely to remit, in middle-aged
212 compared with young adult recipients. We employed an adoptive transfer model in order to distinguish
213 between age-dependent environmental factors in the recipient mouse, as opposed to intrinsic
214 properties of encephalitogenic T cells, that might contribute to the differences in EAE phenotype
215 between the cohorts. The heightened, refractory disability exhibited by older adoptive transfer recipients
216 may reflect an increased vulnerability of aged oligodendrocytes, myelin and/or axons to immune-
217 mediated damage. However, our data indicate that aging has an impact on neuroinflammation itself,
218 since the cellular composition of $CD45^+$ cells in the CNS at peak EAE differs markedly between young
219 adult and middle-aged recipients. Donor T cells and neutrophils were consistently more abundant, while
220 B cells were relatively sparse, in the CNS of older mice. Our experiments with reciprocal bone marrow
221 chimeric mice indicate that radio-resistant, non-hematopoietic cells play a dominant role in shaping
222 age-dependent features of the neuroinflammatory response, as well as the clinical course, during EAE.
223 Among radio-resistant host cells, glia are strong candidates for regulators of CNS autoimmunity.

224 We found that murine microglia spontaneously up-regulate CD11c as they age. This is
225 consistent with previous reports that aging microglia exhibit morphological, phenotypic, and
226 transcriptomic changes indicative of a predisposition towards an activated or pro-inflammatory state
227 (16-18). A number of the pro-inflammatory genes that we identified as upregulated in naive middle-
228 aged, compared with young adult, microglia have previously been reported to be upregulated in
229 microglia from geriatric mice (14). Our working hypothesis is that the increased susceptibility of middle-
230 aged mice to encephalitogenic T cell accumulation, white matter damage, and exacerbated clinical
231 EAE, is driven, at least in part, by aging microglia. Indeed, enhanced microglial reactivity in the aging
232 monkey brain correlates with an increase in perivascular T cell infiltrates in the white matter
233 parenchyma, as well as cognitive impairment (19). Interestingly, genes we found to be highly expressed
234 by microglia from middle aged adoptive transfer recipients are also expressed at high levels by

235 microglia located in the rims of chronic active lesions during pMS, including genes involved in
236 expression of the MHC-II protein complex, ferritin complex, and complement cascade (Supplementary
237 Fig. 3).

238 The mechanisms underlying age-related changes in microglia are likely multifold. Neuronal
239 maintenance of microglial homeostasis via CX3CL1/CX3CR1 and CD200/CD200R interactions wanes
240 with aging (20-22). In addition, microglia can be stimulated by CNS-penetrant, pro-inflammatory factors,
241 such as IL-6, CCL11, and IL-1β, that are systemically released by peripheral immune cells in the
242 context of "inflamm-aging", and/or by microbiome-derived molecules, such as LPS, that rise in the
243 bloodstream consequent to age-related increases in gastrointestinal permeability (17, 18, 23-25).
244 Microbial metabolites, which are altered during dysbiosis, also modulate microglial function in an age-
245 dependent fashion. In young adults, gut microbiome-derived tryptophan metabolites and short chain
246 fatty acids (SCFA) cross the blood-brain-barrier and constitutively suppress microglia, thereby reducing
247 the risk of neuroinflammation (26, 27). Dietary supplementation with the SCFA propionic acid is
248 associated with less inflammatory activity, disability progression, and brain atrophy in MS (28).
249 However, production of SCFAs and tryptophan metabolites by gut bacteria declines with aging (29),
250 thereby removing another check on microglial activation.

251 Single-cell RNA sequencing of $CD45^+$ leukocytes, harvested from the CNS at peak disease,
252 revealed 2 clusters of EAE-associated microglia, both of which exhibit dynamic, age-dependent
253 transcriptomic signatures (Fig. 9). By comparison to their counterparts harvested from young adult
254 adoptive transfer recipients, cluster 1 microglia from middle-aged recipients are highly enriched in
255 transcripts that encode molecules engaged in the presentation of antigen to T cells. This finding led us
256 to hypothesize that more efficient antigen presentation by cluster 1 microglia might boost the
257 proliferation of donor T cells, resulting in higher T cell frequencies within the CNS infiltrates of middle-
258 aged mice. However, contrary to that hypothesis, we found comparable frequencies of $Ki67^+$ donor T
259 cells among $CD45^+$ CNS mononuclear cells isolated from young adult or middle-aged mice at peak

260 EAE (data not shown). Furthermore, $CD45^{int}CD11b^{+}$ microglia, purified from young adult or middle-
261 aged mice at peak EAE, stimulated the proliferation of 2D2 cells (T cell receptor transgenic $CD4^{+}$ cells
262 specific for MOG peptide) to a similar degree (data not shown). To further investigate this issue, in
263 future experiments we will compare the proliferation of donor T cells, and the antigen-presenting/T cell-
264 polarizing capacity of sharply-defined microglial subsets, in young adult versus middle-aged hosts at
265 multiple time-points. Interestingly, some of the transcripts upregulated in cluster 1 microglia from
266 middle-aged mice are involved in the assembly and function of proteasomes and processing of MHC
267 Class I restricted peptides. Although our model of EAE is $CD4^{+}$ T cell-driven, $CD8^{+}$ T cells are more
268 prevalent than $CD4^{+}$ T cells in human MS lesions, including in the chronic active lesions that are typical
269 of pMS (30-32). The emergence of microglia particularly well-equipped to activate $CD8^{+}$ T cells might
270 be relevant to the pathogenesis of pMS.

271 In middle-aged hosts, cluster 2 microglia are enriched in transcripts that encode a range of
272 chemokines including CXCL2 and CXCL10. We and others previously showed that neutrophil migration
273 to the CNS during EAE is dependent on CXCR2-binding chemokines (such as CXCL1, CXCL2)(11, 12,
274 33, 34), while $CD4^{+}$ T cell migration is dependent on CXCR3-binding chemokines (such as CXCL9,
275 CXCL10 and CXCL11) (9). Elevated production of CXCL2 and CXCL10 by aged cluster 2 microglia
276 might trigger preferential accumulation of donor T cells and neutrophils locally, and thereby underlie the
277 relative enrichment of those subpopulations in the CNS of middle-aged hosts during EAE. The
278 translational significance of this finding is underscored by the observations that pMS patients have a
279 relatively high percentage of circulating $CXCR3^{+}$ lymphocytes (35), and $CXCR3^{+}$ lymphocytes
280 preferentially accumulate in MS lesions (36). Furthermore, CXCL9 and CXCL10 are up-regulated in
281 pMS brains[33], and expression of CXCR3 on circulating $CD8^{+}$ T cells correlates with MS lesion volume
282 (37). There is also evidence that neutrophil-related factors and chemokines are dysregulated in pMS
283 and correlate with clinical, as well as radiological, measures of CNS tissue damage (25).

284 In addition to sculpting the neuroinflammatory response via antigen presentation and chemokine
285 production, aging microglia could modulate EAE by releasing soluble factors that directly damage
286 oligodendrocytes and/or axons, such as reactive oxygen and nitrogen species, enzymes and TNF
287 family members (38, 39), and/or that drive the polarization of neurotoxic astrocytes, such as IL-1α and
288 C1q (27, 40). Conversely, we found that aging microglia in cluster 1 downregulate expression of
289 transcripts encoding heat shock proteins 90 and 70, which have been implicated in neuroprotection and
290 the suppression of neurotoxic astrocytes, respectively (41, 42). Increased susceptibility of
291 oligodendrocytes and neurons/axons to immune-mediated insults, combined with impairment of
292 microglial phagocytosis, might escalate CNS deposition of danger-associated molecular patterns
293 (DAMPs) and cellular debris in middle-aged hosts. DAMPs and cellular debris incite the activation of
294 microglia and infiltrating leukocytes, which could fuel a self-amplifying cycle of tissue destruction.
295 Although the adoptive transfer model of EAE in middle-aged mice lacks a number of salient
296 pathological features of pMS (i.e. slowly expanding, chronic active lesions and cortical lesions), it may
297 be useful for investigating how biological aging alters inflammatory demyelinating disease in other ways
298 that simulate progressive MS (i.e. diffuse microglial activation and a non-remitting clinical course), and
299 for testing the efficacy of senolytic drugs, microglial suppressors, or other novel therapeutic
300 interventions potentially beneficial in the pMS subpopulation.

301

302 Methods

303

304 *Mice.*

305 CD45.1 congenic and wild-type C57BL/6 mice were obtained from Charles River Laboratories or the
306 National Cancer Institute. Mice were housed in micro-isolator cages under specific pathogen-free
307 conditions at the Ohio State University. Both male and female mice were used in experiments.

308

309 *Induction and assessment of EAE*.

310 8-12 week old mice were immunized subcutaneously with an emulsion consisting of 100 μg of MOG_{35-55}
311 peptide (MEVGWYRSP-FSRVVHLYRNGK; Biosynthesis) emulsified in Complete Freund's Adjuvant
312 (CFA; Difco), at four sites over the flanks. Inguinal, axial, and brachial lymph nodes and spleens were
313 harvested from donor mice 10-14 days post-immunization and passed through a 70 µm strainer (Fisher
314 Scientific) to obtain a single-cell suspension. The cells were cultured for 96 hours with MOG_{35-55} peptide
315 (50 µg/mL) and Th17-polarizing factors as follows: recombinant murine (rm)IL-23 (8 ng/ml; R&D
316 Systems), rmIL-1α (10 ng/ml; Peprotech) and anti–IFNγ (10 µg/ml; clone XMG1.2, Bio X Cell). After 96
317 hours, the cells were harvested, washed and resuspended in fresh media. $CD4^+$ T cells were purified
318 via positive-selection, magnetic-activated cell sorting (MACS) using L3T4 magnetic microbeads
319 (Miltenyi Biotec) per the manufacturer's protocol. $CD4^+$ T cells (90-98% purity) were transferred via
320 intraperitoneal (i.p.) injection to naïve C57BL/6 recipients. Recipient mice were weighed and observed
321 daily for clinical disability and rated using a 5-point scale as described previously. Briefly, 0.5, partial tail
322 paralysis; 1, full tail paralysis; 1.5, hindlimb weakness demonstrated by ability to correct from a prone
323 position in <1s; 2, hindlimb weakness demonstrated by ability to correct from a prone position in >1s;
324 2.5, hindlimb weakness demonstrated by severe gait abnormality; 3, partial hindlimb paralysis
325 demonstrated by the inability to elevate hindquarters; 3.5 complete paralysis in one hindlimb; 4,
326 complete hindlimb paralysis; 4.5, moribund; and 5, dead.

327

328 *CNS mononuclear cell and homogenate collection.*

329 Mice were anesthetized with isoflurane and perfused with 1x PBS. The brain was removed from the
330 skull, and the spinal cord was flushed through the spinal canal with PBS. Combined brain and spinal
331 cord tissues were homogenized with an 18-gauge needle in a protease inhibitor solution created using

332 protease inhibitor cocktail tablets (Roche) per the manufacturer's protocol, centrifuged at 800 g for 5
333 minutes, and the supernatant was collected and stored at -80°C. Tissue pellet was resuspended in a
334 solution of HBSS with 1 mg/ml collagenase A (Roche) and 1 mg/ml DNase I (Sigma-Aldrich) and
335 incubated at 37°C for 20 minutes. Mononuclear cells were separated from myelin via centrifugation in a
336 27% Percoll solution (GE Healthcare).

337

338 *Fluorescent immunohistochemistry.*

339 Spinal cords were harvested from mice perfused with 1x PBS and 4% paraformaldehyde (PFA). Tissue
340 were post-fixed with 4% PFA for 24 hours, washed with 1x PBS, decalcified with 0.5 M EDTA for 4-6
341 days, and cryopreserved with 30% sucrose solution at 4°C. Tissue was embedded in OCT for
342 cryosectioning and stored at -80°C. Sections were blocked with 5% normal goat serum (Sigma-Aldrich),
343 washed with 0.1% Triton-X 100 (Fisher Scientific) in 1x PBS (PBS-T), and stained with rat anti-mouse
344 CD45 (clone IBL-5/25; EMD Millipore) for 48 hours at 4°C. Following washing with PBS-T, sections
345 were stained with Alexa Fluor 647 goat anti-rat IgG (Invitrogen) for 2 hours. Sections were then stained
346 with FluoroMyelin Red Fluorescent Myelin Stain (Invitrogen) per the manufacturer's protocol. ProLong
347 Gold antifade reagent with DAPI (Invitrogen) was applied immediately prior to applying the coverslip.
348 Images were acquired using an Olympus IX83 inverted fluorescent microscope with cellSens
349 Dimension software (Olympus).

350

351 *Electrophysiology.*

352 Electrophysiological recordings were performed using a clinical electrodiagnostic system (Cadwell).
353 During recordings mice were anesthetized using ketamine/xylazine anesthesia. A petroleum-based eye
354 lubricant (Dechra) was applied to prevent corneal irritation and dryness. A thermostatically-controlled,
355 far infrared heating pad was used to maintain body temperature (Kent Scientific). Hair from the right

356 hindlimb was removed with clippers (Remington, model VPG 6530) to allow for adequate electrode-skin
357 contact. During anesthetized recordings, mice were placed in the prone position, and bilateral hindlimbs
358 were extended and affixed to the heating pad with Transpore medical tape (3M). Compound muscle
359 action potential (CMAP) and single motor unit potential (SMUP) amplitudes were recorded from the
360 right gastrocnemius muscle similar to our prior studies in aged mice(43, 44). Briefly, a pair of recording
361 ring electrodes (Alpine Biomed) were placed at the proximal gastrocnemius (G1) and at the mid-tarsal
362 region of the hind paw (G2). The skin underneath the ring electrodes was coated with electrode gel
363 (Parker Laboratories) to reduce skin impedance. A disposable surface disc electrode was placed on
364 the surface of the skin of the tail (Natus Neurology) as the common reference electrode (G0). Two 28-
365 gauge monopolar electrodes (Natus Neurology) were inserted subcutaneously at the proximal right
366 thigh and used as the cathode and anode to stimulate the sciatic nerve. A constant current stimulator
367 was used to deliver pulses (0-10 mA current, 0.1 ms duration). Supramaximal stimulation was delivered
368 to record the maximum CMAP amplitude. Then the stimulus was reduced, and a gradually increasing
369 stimulus was used to elicit a total of 10 all-or-none CMAP increments. The 10 incremental responses
370 were averaged to determine the average SMUP amplitude which was used to calculate motor unit
371 number estimation (MUNE = maximum CMAP / Average SMUP). To determine CMAP response
372 following spinal cord conduction, the stimulating electrodes were placed subcutaneously at the base of
373 the skull on each side of the spinal column. The spinal cord was stimulated using a constant current
374 stimulator (0-40 mA, 0.2 ms) to elicit the maximum cervical motor evoked potential (MEP) amplitude.
375 During all recordings, high and low frequency filter settings were set at 10 kHz and 10 Hz, respectively.
376 Peak-to-peak amplitudes were used for all analyses.

377

378 *Flow cytometry*

379 For surface staining, cells were resuspended in 1x PBS with 2% fetal bovine serum (FBS), fixable
380 viability dye (eFluor506, eBioscience), and anti-CD16/32 (clone 2.4G2, hybridoma, ATCC). Cells were

381 then labeled with fluorescently labeled monoclonal antibodies specific for individual markers. For
382 intracellular cytokine staining, cells were stimulated with PMA (50 ng/ml), ionomycin (2 μg/ml), and BFA
383 (5 μg/ml) for 4–6 hours. Cells were then fixed and permeabilized with the Fixation/Permeablization Kit
384 (BD Biosciences) according to the manufacturer's protocols and incubated with fluorescently labeled
385 monoclonal antibodies. Data were acquired using a FACSMelody flow cytometer (BD Biosciences) and
386 analyzed with FlowJo software (Tree Star).

387

388 *Antibodies*

389 The following antibodies were obtained from eBiosciences: CD11b (M1/70)- APC-eFluor 780, CD11c
390 (N418)- PerCP-Cyanine5.5, CD45.1 (A20)- FITC and PE, CD45R/B220 (RA3-6B2)- PE, and Ki-67
391 (SolA15)- PE-Cyanine7. The following antibodies were obtained from Invitrogen: CD45 (30-F11)-
392 eFluor 450 and GM-CSF (MP1-22E9)- FITC. The following antibodies were obtained from BD
393 Pharmingen: Ly6G (1A8)- PE-Cy7. The following antibodies were obtained from BioLegend: CD4
394 (RM4-5)- APC. For *in vivo* GM-CSF blocking experiments, 500 μg of anti-mouse GM-CSF (MP1-22E9)
395 or rat IgG2a isotype control (2A3) (Bio X Cell) were administered via i.p. injection.

396

397 *Multiplex cytokine assay*

398 Cytokine levels were measured in spinal cord homogenates by Luminex multiplex bead-based analysis
399 (MILLIPLEX MAP Mouse Cytokine/Chemokine Magnetic Bead Panel; Millipore) using the Bio-Plex 200
400 system (Bio-Rad Laboratories) according to the manufacturer's protocols.

401

402 *Generation of bone marrow chimeras*

403 Femur, tibia, and humorous bones were harvested from donor mice. Marrow was flushed from the
404 bone, passed through a 70 μm mesh filter to generate a single-cell suspension, and red blood cells
405 were lysed by a brief incubation in ACK lysis buffer (Quality Biological). Hosts were lethally irradiated
406 with 2 doses of 6.5 Gy and reconstituted by tail vein injection of 2-4 x 10^6 donor bone marrow cells.
407 Recipient mice were allowed to reconstitute for 6 weeks prior to use.

408

409 *Schematic design*

410 All figure schematics were created using BioRender software.

411

412 *Single-cell RNAseq analysis*

413 Sequence mapping and preprocessing: Mononuclear cells were isolated from 4 spinal cords per group
414 and processed following the 10X Genomics Chromium Single Cell RNA v3 protocol. Libraries were
415 sequenced on an Illumina Novaseq instrument and counted with CellRanger v3.1.0 using mm10
416 reference genome GENCODE vM23/Ensembl 98). Data processing and visualizations of the scRNAseq
417 data were performed using the Seurat package (v.4.0.4) in R (4.1.0). For the initial quality control
418 filtering, we removed individual cells that detected less than 200 genes or more than 25,000 reads, and
419 genes that were detected in less than three cells. We filtered outlier cells outside the range of 5x
420 median absolute deviation of that cell due to sequencing depth using scater. We also only retained cells
421 with less than 10% mitochondrial reads and less than 50% ribosomal reads. Data were scaled to
422 10,000 transcripts per cell, and transformed to log space using Seurat's LogNormalize method. The top
423 2,000 highly variable genes in each sample were computed based on dispersion and mean.

424 Data integration and cell clustering To correct batch effects, anchor genes were identified from all
425 samples using the *FindIntegrationAnchors()* function in Seurat on the first 20 dimensions, and data
426 were integrated via the Seurat *IntegrateData*() function. Principal component analysis (PCA) was

427 performed on the top highly variable genes. The top 20 PCs were used to build a k-nearest-neighbors
428 cell-cell graph with k = 30 neighbors. Cell clusters were identified using the Louvain graph-clustering
429 algorithm with a resolution set to 0.4. We assigned the cell-type labels for each cell cluster using small
430 sets of known marker genes and cluster-specific genes. Finally, the dataset was projected onto two-
431 dimensional space using uniform manifold approximation and projection (UMAP) dimensionality
432 reduction with default parameters.

433 DEG analysis and enrichment test: We identified cluster-specific genes for the clusters using the
434 *FindAllMarkers* function, comparing the gene expression levels in a given cluster with the rest of the
435 cells. The significance of difference was determined using a Wilcoxon Rank Sum test with Bonferroni
436 correction. Differentially expressed genes (DEG) are determined by setting a threshold of the adjusted
437 p-value of < 0.05 and absolute log2-fold change > 0.25. We computationally selected individual cell
438 types for between-group differential gene expression analysis. Note that the batch corrected integration
439 data was only used for cell clustering and dimensional reduction, and the differential gene expression
440 analysis was performed using the normalized RNA assay slot in Seurat. Pathway enrichment analysis
441 was performed using Enrichr using libraries including GO_2018 and KEGG_2019_MOUSE. We also
442 used clusterProfiler's universal enrichment analyzer to analyze our manually selected GO pathways
443 and overlapping DEGs with public datasets. Volcano plots were generated for DEG visualization using
444 EnhancedVolcano. Heatmaps were generated using ComplexHeatmap on z-score transformed
445 normalized gene expression values.

446 Data availability: Single-cell RNA-seq data will be available in the Gene Expression Omnibus (GEO)
447 database upon acceptance of the manuscript.

448

449 *Bulk RNA-seq analysis*

450 Individual FASTQ files were trimmed for adapter sequences and filtered using fastp v0.20.0. Mouse
451 reference genome GRCm38.p6 and gene annotation described by Gene Transfer Format (GTF) were
452 downloaded from Ensembl release 99 (January 2020). Reads alignment was performed against the
453 reference genome using HISAT2 v2.1.0. Gene expression values for genes were quantified using the
454 featureCounts tool of the Subread package v1.5.0-p2 in the unstranded mode. Genes detected in less
455 than ten total counts in at least three samples were removed from downstream analysis. The fold-
456 change was calculated using CPM-normalized values using EdgeR.

457

458 *Statistical analysis of clinical, proteomics and flow cytometric data*

459 Statistical analysis was performed in GraphPad Prism using paired or unpaired 2-tailed Student's t test,
460 or 1-way or 2-way ANOVA with correction for multiple comparisons, as indicated in the legends.
461 Disease curves were compared by unpaired t tests with a Welch correction at individual days where
462 indicated. Comparison for incidence, survival, and remission curves were performed using a Log-rank
463 test. Outliers were identified by ROUT analysis and removed as necessary. A p value less than 0.05 (*)
464 was considered significant; **p <0.01, ***p <0.001, and ****p <0.0001. Statistical analysis used in
465 RNAseq analysis is provided in the previous subsection.

466

467 *Study approval*

468 All animal experiments were performed in accordance with an IACUC-approved protocol at The Ohio
469 State University.

470

471 ## Author Contributions

472 J.R.A., A.D.J., A.R.S., A. Munie, and W.D.A. performed experiments and data analysis. A. Ma and
473 C.W. oversaw RNAseq analysis. B.M.S. and J.R.A. wrote the manuscript and coedited it with the help
474 of the other authors. B.M.S. and J.R.A. directed the studies.

475

476 Acknowledgements

477 We thank R. Yousef and A. McVey Moffatt for technical support. This work was supported by National
478 Institute of Neurological Disorders and Stroke grant R01 NS105385 (to BMS). BMS is the Stanley and
479 Joan D. Ross Professor of Neuromodulation.

480 ## References

481 1. Lassmann H. Pathogenic Mechanisms Associated With Different Clinical Courses of Multiple
482 Sclerosis. *Front Immunol.* 2018;9:3116.
483 2. Frischer JM, Weigand SD, Guo Y, Kale N, Parisi JE, Pirko I, et al. Clinical and pathological
484 insights into the dynamic nature of the white matter multiple sclerosis plaque. *Ann Neurol.*
485 2015;78(5):710-21.
486 3. Tutuncu M, Tang J, Zeid NA, Kale N, Crusan DJ, Atkinson EJ, et al. Onset of progressive phase
487 is an age-dependent clinical milestone in multiple sclerosis. *Mult Scler.* 2013;19(2):188-98.
488 4. Harding KE, Liang K, Cossburn MD, Ingram G, Hirst CL, Pickersgill TP, et al. Long-term
489 outcome of paediatric-onset multiple sclerosis: a population-based study. *J Neurol Neurosurg*
490 *Psychiatry.* 2013;84(2):141-7.
491 5. Tremlett H, Zhao Y, Joseph J, Devonshire V, and Neurologists UC. Relapses in multiple
492 sclerosis are age- and time-dependent. *J Neurol Neurosurg Psychiatry.* 2008;79(12):1368-74.
493 6. Rao P, and Segal BM. Experimental autoimmune encephalomyelitis. *Methods Mol Med.*
494 2004;102:363-75.
495 7. Segal BM. CNS chemokines, cytokines, and dendritic cells in autoimmune demyelination. *J*
496 *Neurol Sci.* 2005;228(2):210-4.
497 8. Dutta S, and Sengupta P. Men and mice: Relating their ages. *Life Sci.* 2016;152:244-8.
498 9. Lalor SJ, and Segal BM. Th1-mediated experimental autoimmune encephalomyelitis is CXCR3
499 independent. *Eur J Immunol.* 2013;43(11):2866-74.
500 10. Hamann I, Zipp F, and Infante-Duarte C. Therapeutic targeting of chemokine signaling in
501 Multiple Sclerosis. *Journal of the Neurological Sciences.* 2008;274(1-2):31-8.
502 11. Carlson T, Kroenke M, Rao P, Lane TE, and Segal B. The Th17-ELR+ CXC chemokine
503 pathway is essential for the development of central nervous system autoimmune disease. *J Exp*
504 *Med.* 2008;205(4):811-23.

505 12. Kroenke MA, Chensue SW, and Segal BM. EAE mediated by a non-IFN-gamma/non-IL-17
506 pathway. *Eur J Immunol.* 2010;40(8):2340-8.
507 13. Duncker PC, Stoolman JS, Huber AK, and Segal BM. GM-CSF Promotes Chronic Disability in
508 Experimental Autoimmune Encephalomyelitis by Altering the Composition of Central Nervous
509 System-Infiltrating Cells, but Is Dispensable for Disease Induction. *J Immunol.* 2018;200(3):966-
510 73.
511 14. Hammond TR, Dufort C, Dissing-Olesen L, Giera S, Young A, Wysoker A, et al. Single-Cell
512 RNA Sequencing of Microglia throughout the Mouse Lifespan and in the Injured Brain Reveals
513 Complex Cell-State Changes. *Immunity.* 2019;50(1):253-71 e6.
514 15. Mrdjen D, Pavlovic A, Hartmann FJ, Schreiner B, Utz SG, Leung BP, et al. High-Dimensional
515 Single-Cell Mapping of Central Nervous System Immune Cells Reveals Distinct Myeloid
516 Subsets in Health, Aging, and Disease. *Immunity.* 2018;48(2):380-95 e6.
517 16. Wynne AM, Henry CJ, and Godbout JP. Immune and behavioral consequences of microglial
518 reactivity in the aged brain. *Integr Comp Biol.* 2009;49(3):254-66.
519 17. Perry VH, and Holmes C. Microglial priming in neurodegenerative disease. *Nat Rev Neurol.*
520 2014;10(4):217-24.
521 18. von Bernhardi R, Eugenin-von Bernhardi L, and Eugenin J. Microglial cell dysregulation in brain
522 aging and neurodegeneration. *Front Aging Neurosci.* 2015;7:124.
523 19. Batterman KV, Cabrera PE, Moore TL, and Rosene DL. T Cells Actively Infiltrate the White
524 Matter of the Aging Monkey Brain in Relation to Increased Microglial Reactivity and Cognitive
525 Decline. *Front Immunol.* 2021;12:607691.
526 20. Gyoneva S, Hosur R, Gosselin D, Zhang B, Ouyang Z, Cotleur AC, et al. Cx3cr1-deficient
527 microglia exhibit a premature aging transcriptome. *Life Sci Alliance.* 2019;2(6).
528 21. Manich G, Recasens M, Valente T, Almolda B, Gonzalez B, and Castellano B. Role of the
529 CD200-CD200R Axis During Homeostasis and Neuroinflammation. *Neuroscience.*
530 2019;405:118-36.

531 22. Wynne AM, Henry CJ, Huang Y, Cleland A, and Godbout JP. Protracted downregulation of
532 CX3CR1 on microglia of aged mice after lipopolysaccharide challenge. *Brain Behav Immun.*
533 2010;24(7):1190-201.
534 23. Manabe T, Racz I, Schwartz S, Oberle L, Santarelli F, Emmrich JV, et al. Systemic inflammation
535 induced the delayed reduction of excitatory synapses in the CA3 during ageing. *J Neurochem.*
536 2021;159(3):525-42.
537 24. Huber AK, Giles DA, Segal BM, and Irani DN. An emerging role for eotaxins in
538 neurodegenerative disease. *Clin Immunol.* 2018;189:29-33.
539 25. Huber AK, Wang L, Han P, Zhang X, Ekholm S, Srinivasan A, et al. Dysregulation of the IL-
540 23/IL-17 axis and myeloid factors in secondary progressive MS. *Neurology.* 2014;83(17):1500-
541 7.
542 26. Haghikia A, Jorg S, Duscha A, Berg J, Manzel A, Waschbisch A, et al. Dietary Fatty Acids
543 Directly Impact Central Nervous System Autoimmunity via the Small Intestine. *Immunity.*
544 2015;43(4):817-29.
545 27. Rothhammer V, Borucki DM, Tjon EC, Takenaka MC, Chao CC, Ardura-Fabregat A, et al.
546 Microglial control of astrocytes in response to microbial metabolites. *Nature.*
547 2018;557(7707):724-8.
548 28. Duscha A, Gisevius B, Hirschberg S, Yissachar N, Stangl GI, Eilers E, et al. Propionic Acid
549 Shapes the Multiple Sclerosis Disease Course by an Immunomodulatory Mechanism. *Cell.*
550 2020;180(6):1067-80 e16.
551 29. Ruiz-Ruiz S, Sanchez-Carrillo S, Ciordia S, Mena MC, Mendez-Garcia C, Rojo D, et al.
552 Functional microbiome deficits associated with ageing: Chronological age threshold. *Aging Cell.*
553 2020;19(1):e13063.
554 30. Mockus TE, Munie A, Atkinson JR, and Segal BM. Encephalitogenic and Regulatory CD8 T
555 Cells in Multiple Sclerosis and Its Animal Models. *J Immunol.* 2021;206(1):3-10.

556 31. Booss J, Esiri MM, Tourtellotte WW, and Mason DY. Immunohistological analysis of T
557 lymphocyte subsets in the central nervous system in chronic progressive multiple sclerosis. *J*
558 *Neurol Sci.* 1983;62(1-3):219-32.
559 32. Machado-Santos J, Saji E, Troscher AR, Paunovic M, Liblau R, Gabriely G, et al. The
560 compartmentalized inflammatory response in the multiple sclerosis brain is composed of tissue-
561 resident CD8+ T lymphocytes and B cells. *Brain.* 2018;141(7):2066-82.
562 33. Stoolman JS, Duncker PC, Huber AK, Giles DA, Washnock-Schmid JM, Soulika AM, et al. An
563 IFNgamma/CXCL2 regulatory pathway determines lesion localization during EAE. *J*
564 *Neuroinflammation.* 2018;15(1):208.
565 34. Stoolman JS, Duncker PC, Huber AK, and Segal BM. Site-specific chemokine expression
566 regulates central nervous system inflammation and determines clinical phenotype in
567 autoimmune encephalomyelitis. *J Immunol.* 2014;193(2):564-70.
568 35. Balashov KE, Rottman JB, Weiner HL, and Hancock WW. CCR5(+) and CXCR3(+) T cells are
569 increased in multiple sclerosis and their ligands MIP-1alpha and IP-10 are expressed in
570 demyelinating brain lesions. *Proc Natl Acad Sci U S A.* 1999;96(12):6873-8.
571 36. Simpson JE, Newcombe J, Cuzner ML, and Woodroofe MN. Expression of the interferon-
572 gamma-inducible chemokines IP-10 and Mig and their receptor, CXCR3, in multiple sclerosis
573 lesions. *Neuropathol Appl Neurobiol.* 2000;26(2):133-42.
574 37. Fox RJ, Kivisakk P, Fisher E, Tucky B, Lee JC, Rudick RA, et al. Multiple sclerosis: chemokine
575 receptor expression on circulating lymphocytes in correlation with radiographic measures of
576 tissue injury. *Mult Scler.* 2008;14(8):1036-43.
577 38. Marzan DE, Brugger-Verdon V, West BL, Liddelow S, Samanta J, and Salzer JL. Activated
578 microglia drive demyelination via CSF1R signaling. *Glia.* 2021;69(6):1583-604.
579 39. Clark KC, Josephson A, Benusa SD, Hartley RK, Baer M, Thummala S, et al. Compromised
580 axon initial segment integrity in EAE is preceded by microglial reactivity and contact. *Glia.*
581 2016;64(7):1190-209.

582 40. Liddelow SA, Guttenplan KA, Clarke LE, Bennett FC, Bohlen CJ, Schirmer L, et al. Neurotoxic
583 reactive astrocytes are induced by activated microglia. *Nature.* 2017;541(7638):481-7.
584 41. Calderwood SK, Borges TJ, Eguchi T, Lang BJ, Murshid A, Okusha Y, et al. Extracellular Hsp90
585 and protection of neuronal cells through Nrf2. *Biochem Soc Trans.* 2021;49(5):2299-306.
586 42. Yu WW, Cao SN, Zang CX, Wang L, Yang HY, Bao XQ, et al. Heat shock protein 70
587 suppresses neuroinflammation induced by alpha-synuclein in astrocytes. *Mol Cell Neurosci.*
588 2018;86:58-64.
589 43. Chugh D, Iyer CC, Wang X, Bobbili P, Rich MM, and Arnold WD. Neuromuscular junction
590 transmission failure is a late phenotype in aging mice. *Neurobiol Aging.* 2020;86:182-90.
591 44. Sheth KA, Iyer CC, Wier CG, Crum AE, Bratasz A, Kolb SJ, et al. Muscle strength and size are
592 associated with motor unit connectivity in aged mice. *Neurobiol Aging.* 2018;67:128-36.

593

594

595

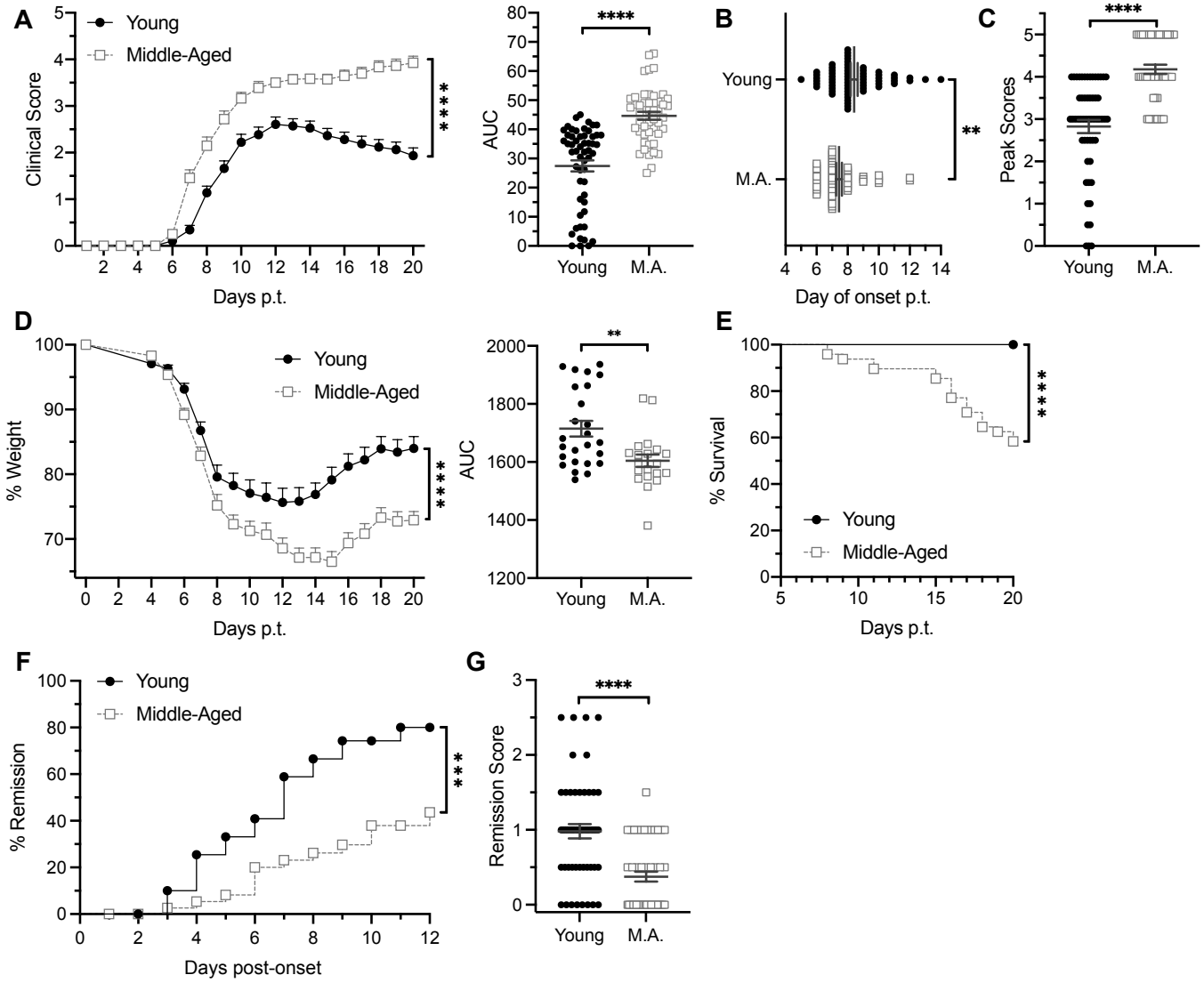

Figure 1. Middle-aged mice exhibit an exacerbated, non-remitting course of Th17-mediated EAE. EAE was induced by the adoptive transfer of myelin-reactive Th17 cells into young or middle-aged mice. (**A-C**) Young (n=70) and middle-aged (n=62) adoptive transfer recipients were scored daily for severity of neurological deficits by an examiner blinded to the identity of experimental groups. Data were pooled from 4 independent experiments. (**A**) Mean clinical scores of young and middle-aged hosts over time (left panel). The area under the curve (AUC) was measured for individual mice in each group (right panel). (**B**) Day of disease onset post-transfer (p.t.) and (**C**) peak clinical disease scores of individual mice. (**D**) Young (n=40) and middle aged (n=36) recipients were weighed on a daily basis. Data were pooled from 3 independent experiments. The % of baseline weight over time, averaged across young and middle-aged recipients (left panel). The area under the curve (AUC) was measured for individual mice in each group (right panel). (**E**) Percent survival over the disease course. (**F**) Percent of mice undergoing remission on each day post clinical onset (left panel). (**H**) Difference between clinical score at peak disease minus score at day 20 post- cell transfer for each mouse. Each symbol in **B** and **C**, and the right panels of **A**, **D**, and **F**, represents data generated from a single mouse. Statistical significance was determined using unpaired 2-tailed Student's *t* test. Curves in the left panels of **A** and **D** were compared using a mixed effects model. Curves in **F** and **G** were compared using the Log rank test. Error bars indicate mean ± SEM. *p <0.05, **p <0.01, ***p <0.001, ****p <0.0001.

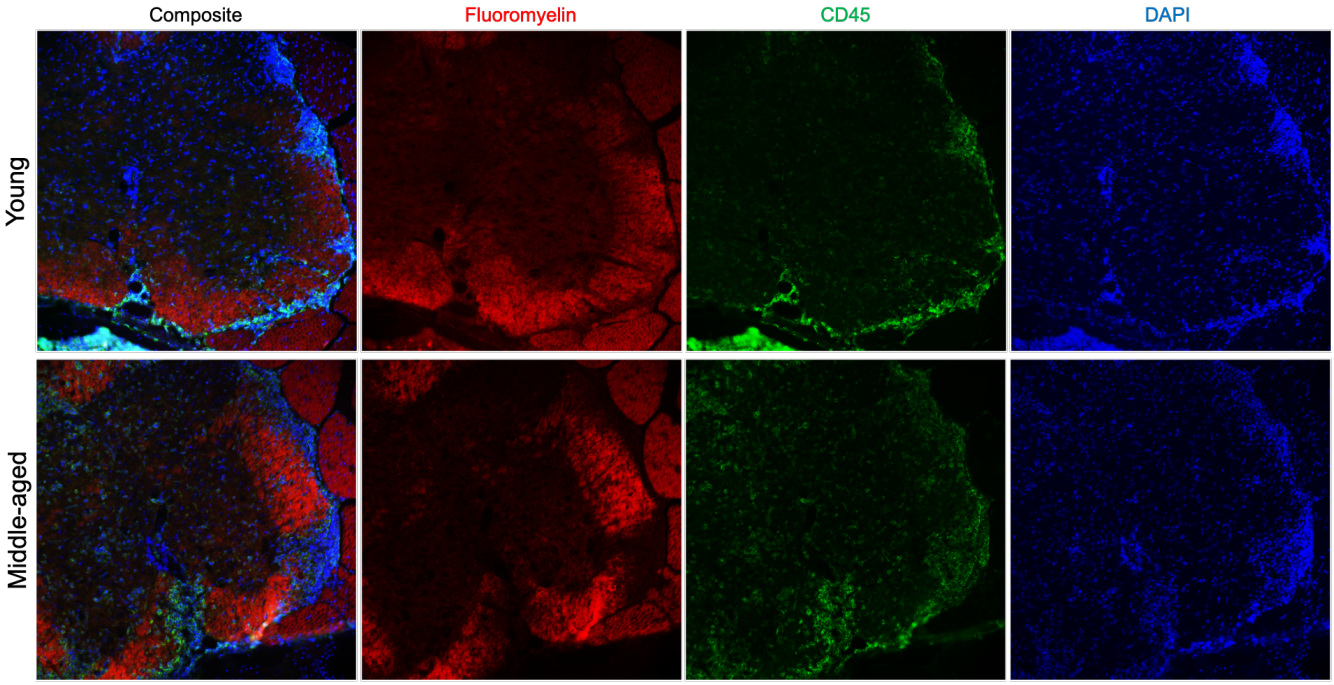

614

615 **Figure 2. Spinal cord demyelination and inflammatory infiltration are exacerbated in middle-aged**
616 **recipients.** Representative spinal cord sections of young (upper panels) and middle-aged (lower panels) adoptive
617 transfer recipients of encephalitogenic Th17 cells. Sections were stained for myelin (Fluoromyelin; red), CD45
618 (green), and DAPI (blue). All images were acquired at 20x magnification.

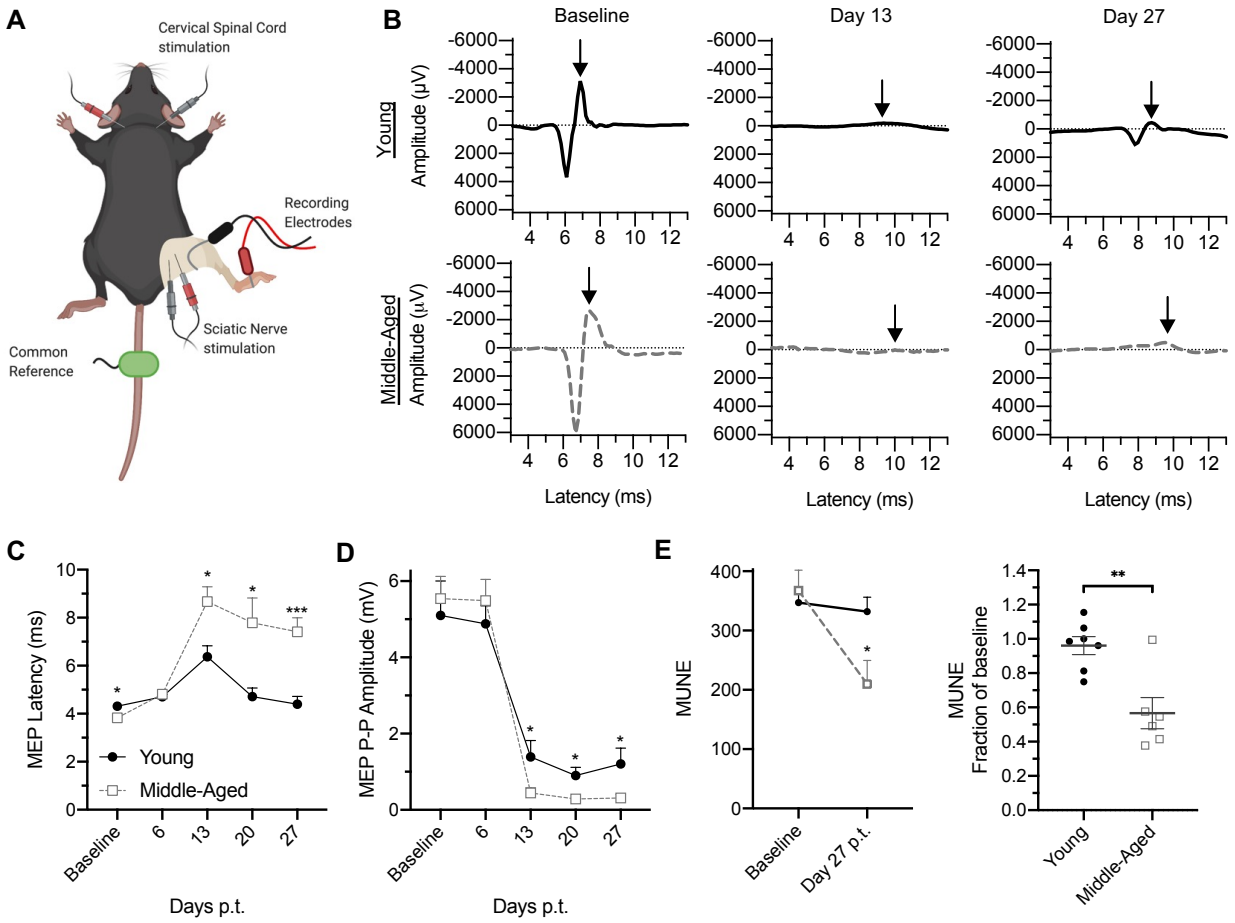

Figure 3. Electrophysiological studies indicate increased demyelination and neuronal/axonal drop out in the spinal cords of middle-aged mice with EAE. (**A-E**) EAE was induced in young adult (n=10) and middle-aged (n=10) mice by the adoptive transfer of encephalitogenic MOG-specific CD4+ T cells. Mice were anaesthetized for electrographic recordings. (**A**) Depiction of electrode placement. (**B**) Representative cervical motor-evoked potentials recorded from the right gastrocnemius following cervical spinal cord stimulation at baseline, day 13, and day 27 post-cell transfer. Arrows indicate negative peaks of the cervical motor-evoked potentials. (**C, D**) Electrographic measurements were obtained at baseline and then on a weekly basis post-transfer (p.t.). Measurements of motor-evoked potential latency (**C**), and peak-to-peak (P-P) amplitude (**D**) were averaged across each group. (**E**) Motor unit number estimation (MUNE) was calculated at baseline and on day 27 post transfer. Mean values for each group are shown (left panel). The ratio of MUNE at day 27 post-cell transfer over baseline is shown for individual mice (right panel). Statistical significance determined by unpaired 2-tailed Student's *t* test. *p <0.05, **p <0.01, ***p <0.001. Error bars indicate mean ± SEM.

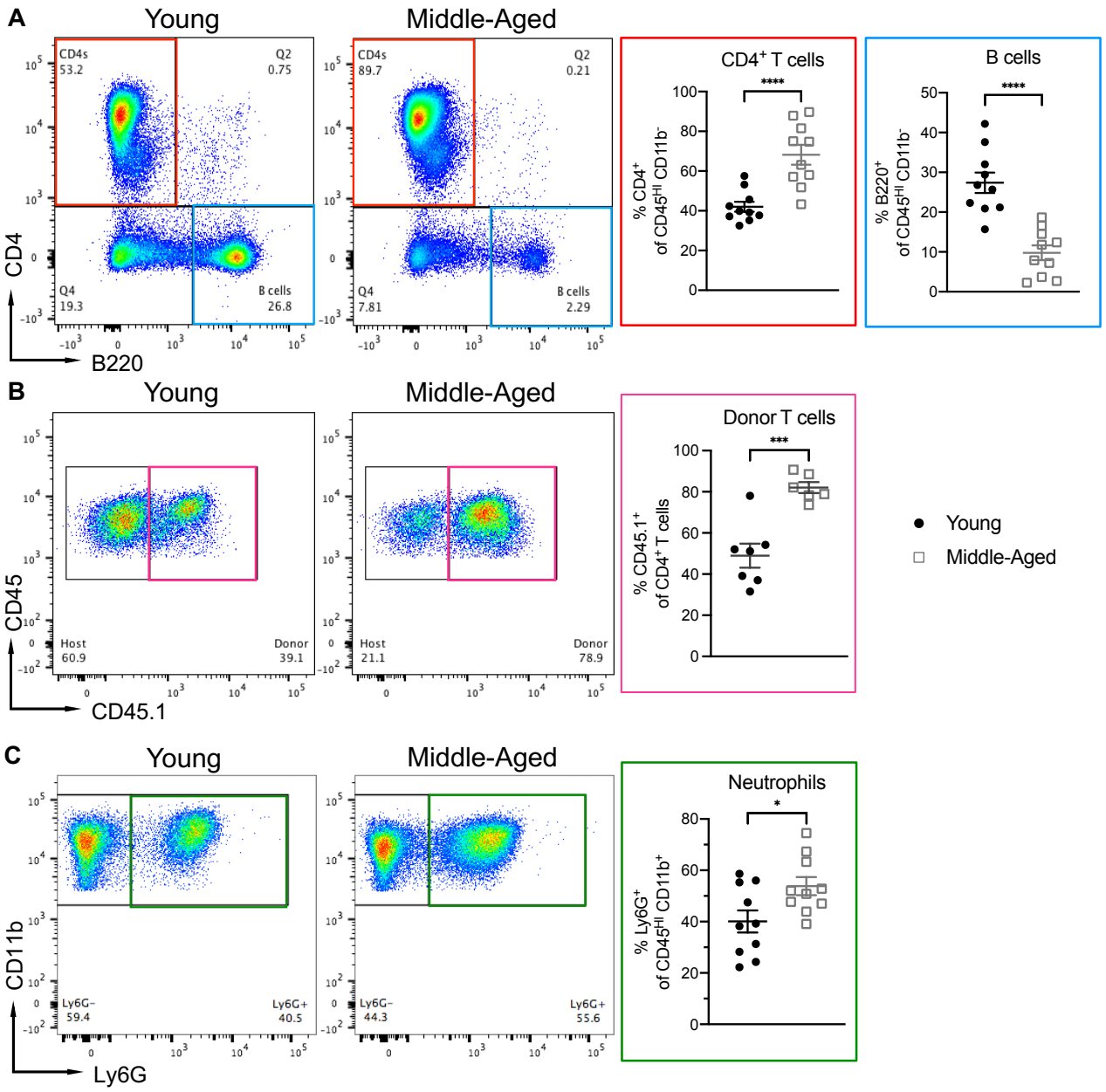

Figure 4. The composition of CNS-infiltrating immune cells differs between middle-aged and young adult mice with EAE. (**A-C**) Mononuclear cells were isolated from the spinal cords of young adult and middle-aged mice on day 10 post-transfer of encephalitogenic CD45.1$^+$ CD4$^+$ T cells for flow cytometric analysis, gating on all CD45$^+$ cells. Representative dot plots (left panels). The frequencies of CD4$^+$ T cells and B cells (**A**), CD45.1$^+$ donor CD4+ T cells (**B**), and neutrophils (**C**), among CNS-infiltrating CD45$^+$ cells (right panels). Each symbol represents an individual mouse. Data were pooled from 3 independent experiments with a total of 7-10 mice per group. Statistical significance was determined using the unpaired 2-tailed Student's *t* test. *p <0.05, ***p <0.001, ****p <0.0001. Error bars indicate mean ± SEM.

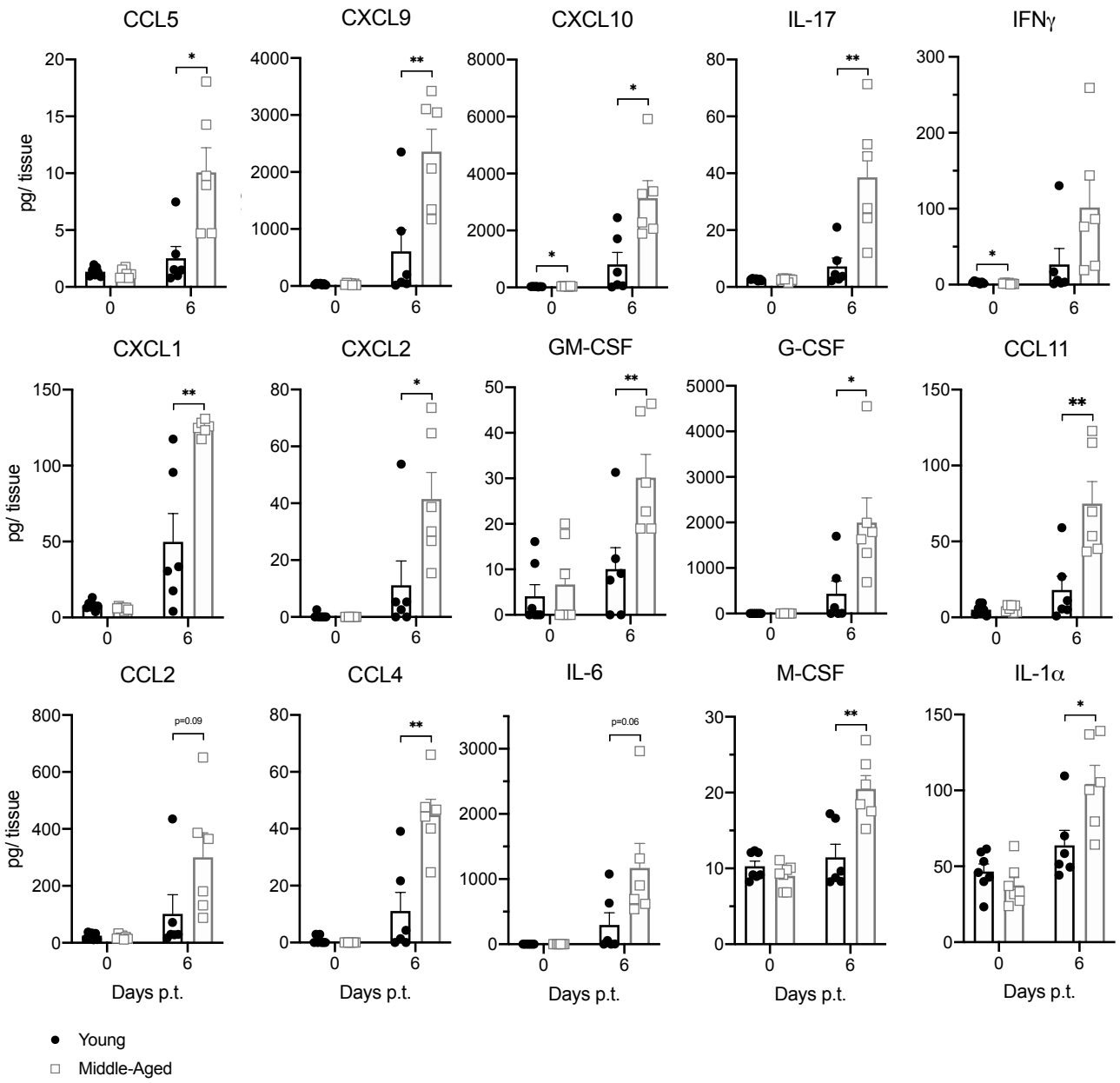

Figure 5. Pro-inflammatory proteins and elevated in the spinal cords of middle-aged mice with adoptive transfer EAE. Spinal cord homogenates were obtained from young (closed circles) and middle-aged (open squares) naïve mice (left bars) or adoptive transfer recipients on day 6 post-transfer (right bars). A panel of pro-inflammatory factors were measured using the Luminex bead-based multiplex platform. Data were pooled from 2-4 independent experiments with a total of 7-13 mice/group. Each symbol represents a single mouse. Statistical significance was determined using the unpaired 2-tailed Student's *t* test. *p <0.05, ***p <0.001, ****p <0.0001. Error bars indicate mean ± SEM.

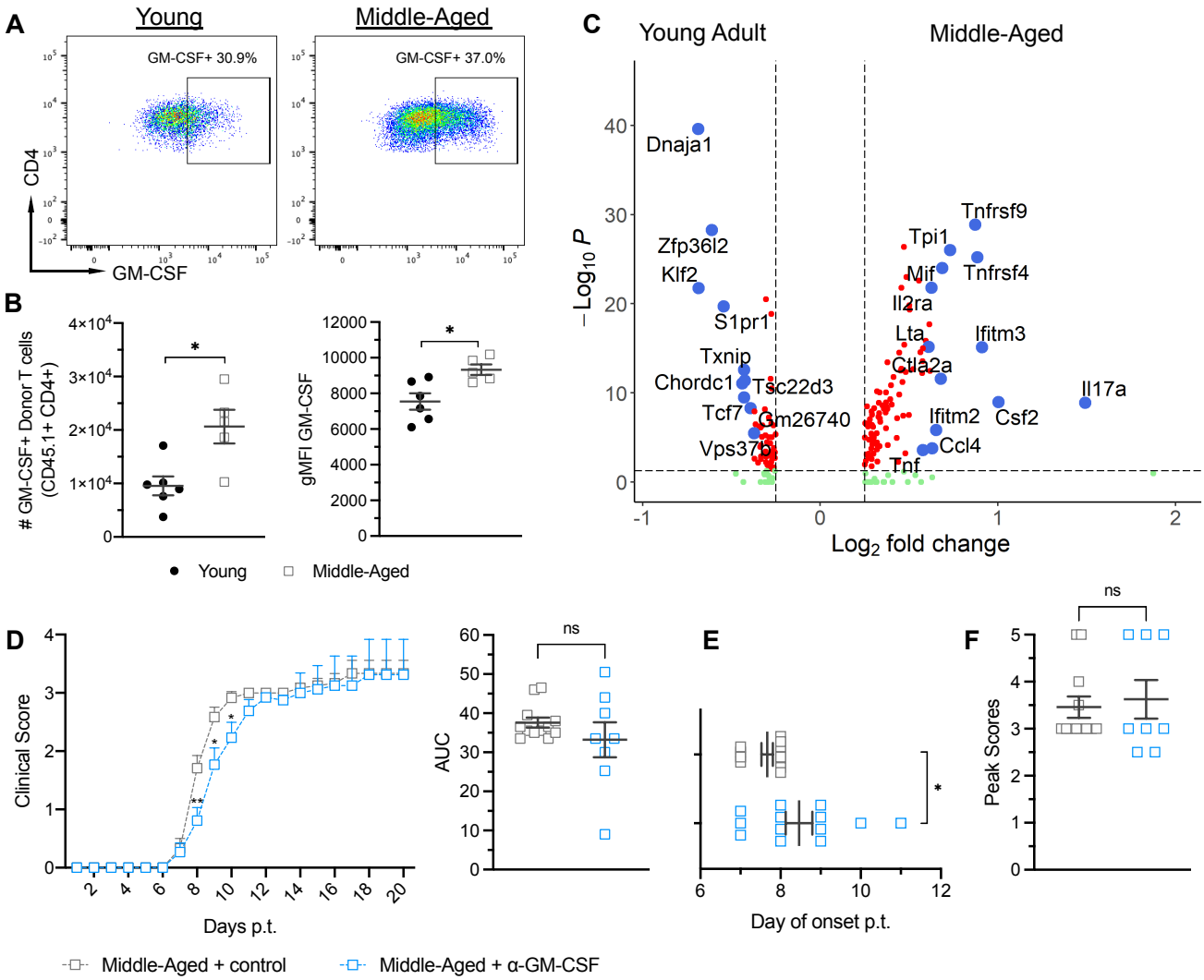

Figure 6. GM-CSF promotes exacerbated EAE in middle-aged mice early, but not late, in the clinical course. (**A, B**) CNS mononuclear cells were harvested from the spinal cords of young adult and middle-aged mice on day 10 post-T cell transfer for analysis by flow cytometry. (**A**) Representative dot plots showing intracellular GM-CSF expression, gating on CD45.1$^+$ donor CD4$^+$ T cells. (**B**) Total number of GM-CSF$^+$ donor T cells (left panel), and geometric mean fluorescent intensity (gMFI) of GM-CSF in donor T cells (right panel), isolated from the spinal cords of individual mice. Data were pooled from 2 independent experiments with 5-6 mice/group. (**C**) CD45$^+$ mononuclear cells, FACS sorted from young adult or middle-aged mice with EAE on day 6 post-cell transfer, were analyzed by scRNAseq. Gene expression changes in CNS CD4+ T cells, comparing young and middle aged mice, are shown in a volcano plot. (**D-F**) Middle-aged mice were injected i.p. with anti-GM-CSF neutralizing antibody or control antibody every other day from the time of encephalitogenic T cell transfer onward (n= 14 mice/group; pooled from 2 independent experiments). Mice were scored for severity of neurological deficits on a daily basis by raters blinded to the identity of the experimental groups. (**D**) Mean clinical scores of mice in each group over time (left panel). Area under the curves (AUC) of individual mice (right panel). (**E**) Day of clinical disease onset post-transfer and (**F**) peak clinical disease scores of individual mice. Statistical significance was determined using the unpaired 2-tailed Student's *t* test. *p <0.05 or as indicated. Error bars indicate mean ± SEM.

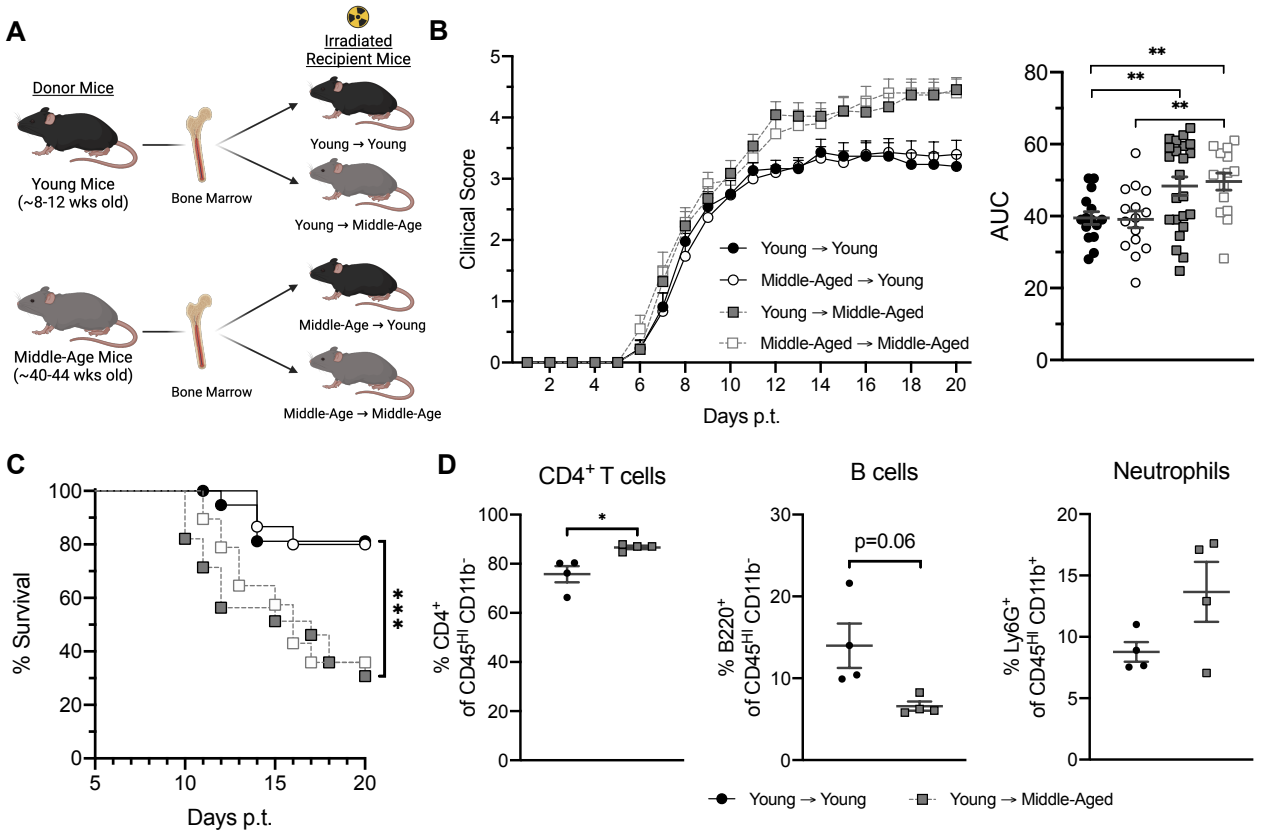

Figure 7. Radio-resistant, non-hematopoietic cells drive exacerbated EAE in middle-aged mice. (**A-D**) Reciprocal bone marrow chimeric mice were constructed with young adult or middle-aged donors and hosts. Following reconstitution, all chimeric mice were injected i.p. with 3 x 10^6 MOG-primed $CD4^+$ Th17 cells. Mice were scored for severity of neurological deficits on a daily basis by raters blinded to the identity of the experimental groups. (**A**) Schematic depicting the construction of reciprocal bone marrow chimeras. (**B**) Mean clinical scores over time (left panel) and area under the curves (AUC) of individual mice (right panel). (**C**) Percent of surviving mice in each group over time. (**D**) Frequencies of $CD4^+$ T cells, B cells, and neutrophils among $CD45^+$ spinal cord mononuclear cells harvested from individual mice on day 10 post-transfer. Data in (**B**) and (**C**) were pooled from 3 independent experiments with a total of 15-28 mice per group. Each symbol in B, right panel, and in D represent an individual mouse, Data in (**D**) are representative experiment of 3 independent experiments (n=4 mice/group). Statistical significance was determined using the unpaired 2-tailed Student's *t* test. Curves in **C** were compared using the Log rank test. *p <0.05, **p <0.01, ***p <0.001 or as indicated. Error bars indicate mean ± SEM.

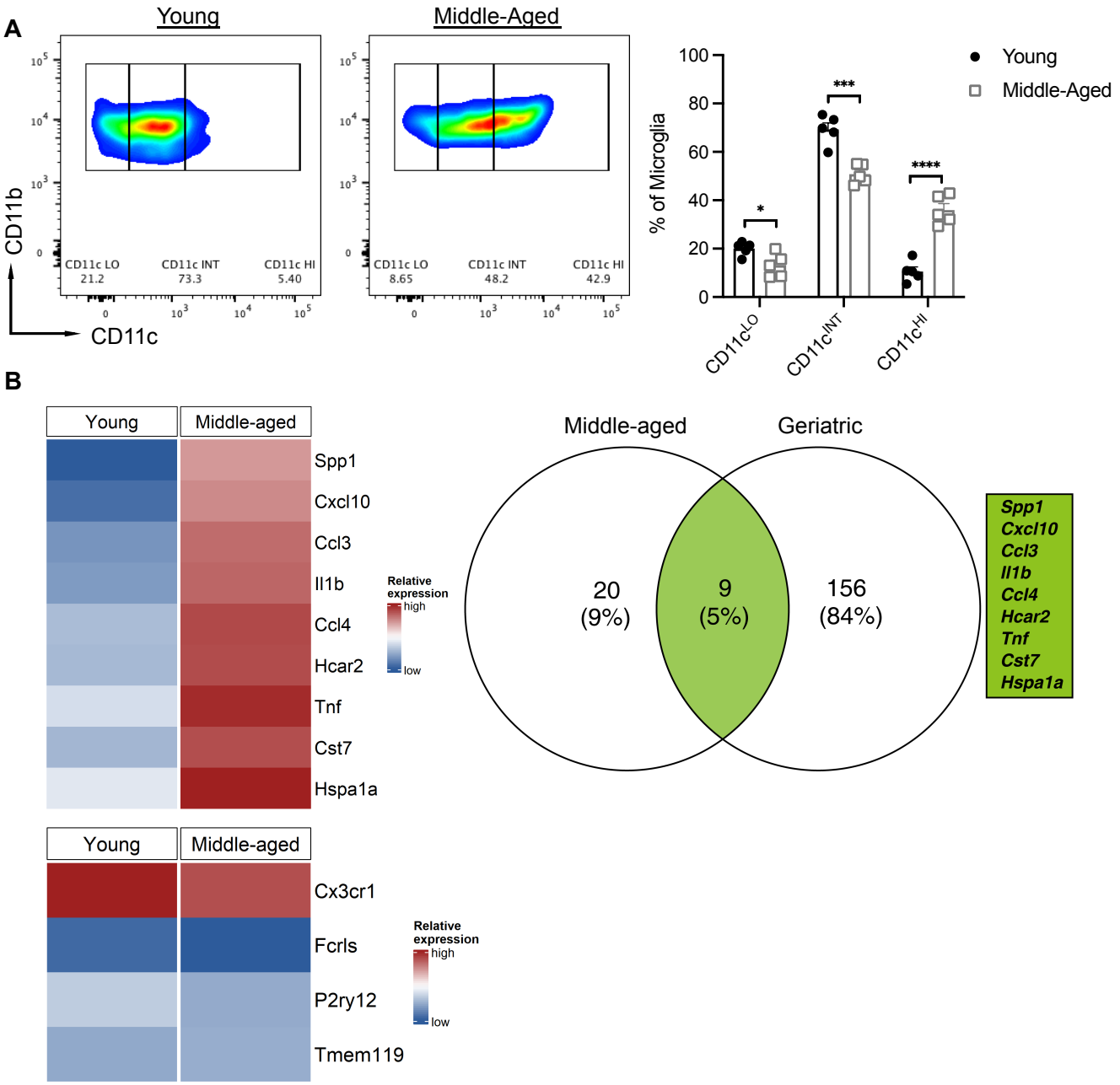

Figure 8. Microglia in middle-aged mice up-regulate genes indicative of a reactive, age-associated phenotype. Mononuclear cells were harvested from the spinal cords of naïve young adult and middle-aged mice. (**A**) Representative dot plots (left and middle panel), and frequencies of CD11c^{lo}, CD11c^{int} and CD11c^{hi} cells among CD45^{int}CD11b+ microglia (right panel), are shown. Each symbol in the right panel represents an individual mouse. Data were pooled from 2 independent experiments with n=5 mice/group. Statistical significance was determined using the unpaired 2-tailed Student's *t* test. *p <0.05, ***p <0.001, ****p <0.0001. Error bars indicate mean ± SEM. (**B**) CD45^{INT} CD11b+ cells were FACS sorted and RNA was extracted for bulk sequencing. Venn diagram depicts the number of overlapping genes and overall percent of genes up-regulated in naïve microglia isolated from middle-aged mice compared to geriatric mice (age P540) (left). Heat maps illustrating the relative expression of overlapping genes (right) and homeostatic genes (bottom).

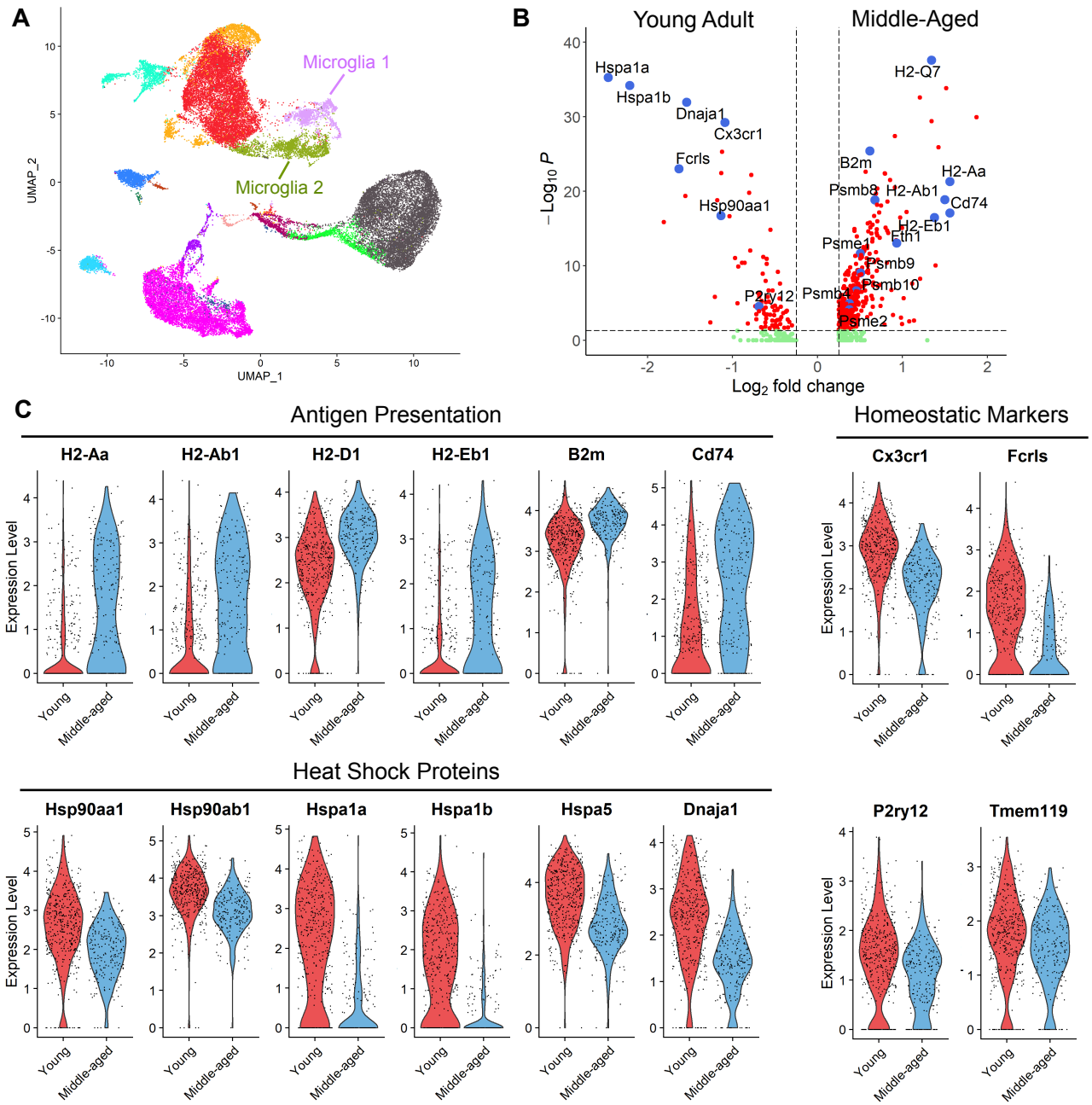

Figure. 9. Microglia from middle-aged mice with EAE express distinct transcriptomic signatures. CD45$^+$ mononuclear cells were FACS sorted from young adult or middle aged mice with EAE on day 6 post-cell transfer and subjected to scRNA-seq. (**A**) Unified manifold approximation and projection (UMAP) plot showing clustering by cell type, labeled on the basis of known lineage markers. **(B**) Gene expression changes in cluster 1 microglia isolated from young adult versus middle-aged mice, shown as a volcano plot. (**C**) Selected differentially expressed genes in cluster 1 microglia from young adult (red) and middle-aged (blue) adoptive transfer recipients, shown as violin pots. Numbers on the y-axis correspond to the z score for each gene.

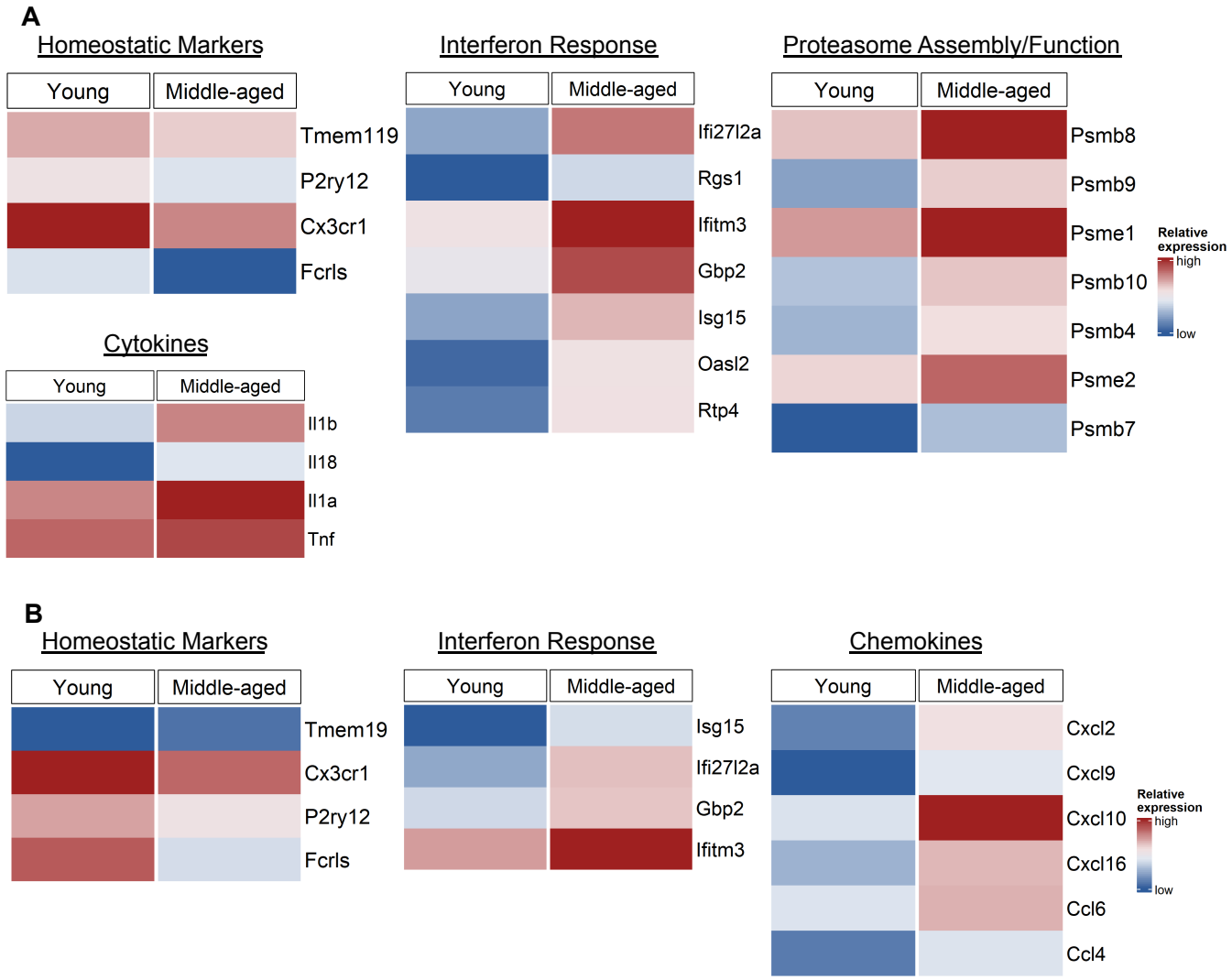

Figure 10. Microglia from middle-aged mice with EAE down-regulate homeostatic genes and up-regulate pro-inflammatory and IFN response genes. Single-cell RNA-sequencing was performed on CD45^{+} CNS mononuclear cells isolated from young adult and middle-aged adoptive transfer recipients as described in the legend to Figure 9. The heat maps show z-score transformed normalized expression values of selected genes in cluster 1 microglia (**A**) or cluster 2 microglia (**B**), comparing young adult and middle-aged recipient mice.

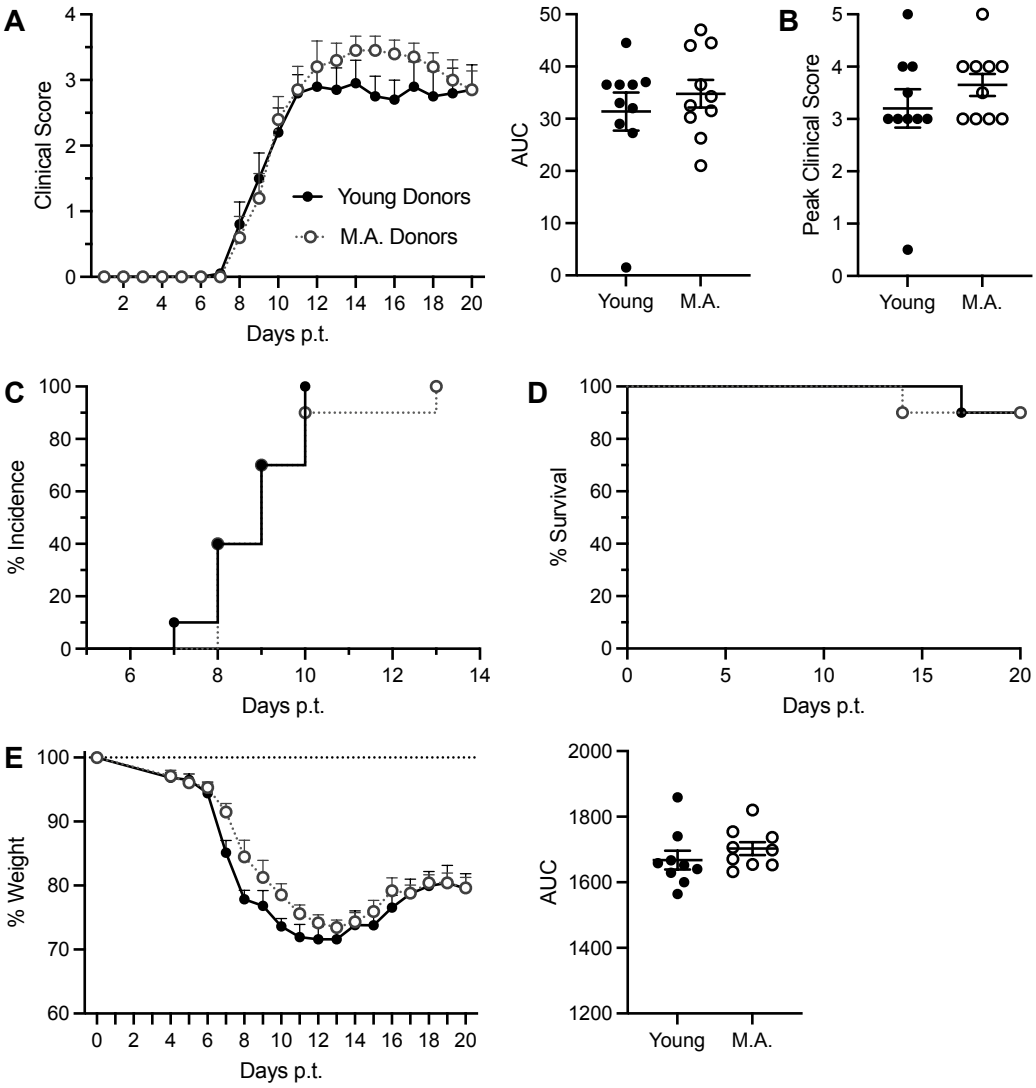

706

707 **Supplementary Figure 1. The age of MOG-primed donor CD4+ T cells does not impact the clinical course**
708 **of adoptively transferred EAE.** MOG/CFA primed lymph node cells from young adult (8-12 week old) or middle-
709 age (M.A., 40-44 week old) mice were cultured with MOG_{35-55} peptide and Th17 polarizing factors. The cells were
710 harvested 96 hours later. CD4+ T cells were purified and injected into naïve, syngeneic young adult mice (n=10
711 mice/ group). (**A**) Mean clinical scores of mice in each group (left) and areas under the curve (AUC) of individual
712 mice (right). (**B**) Peak clinical scores for individual mice. (**C**) Disease incidence in each group over time. (**E**)
713 Percent of surviving mice in each group over time. (**E**) Mean change in weight (shown as percent of baseline
714 weight) of mice in each group throughout the clinical course (left), and AUCs of individual mice (right).

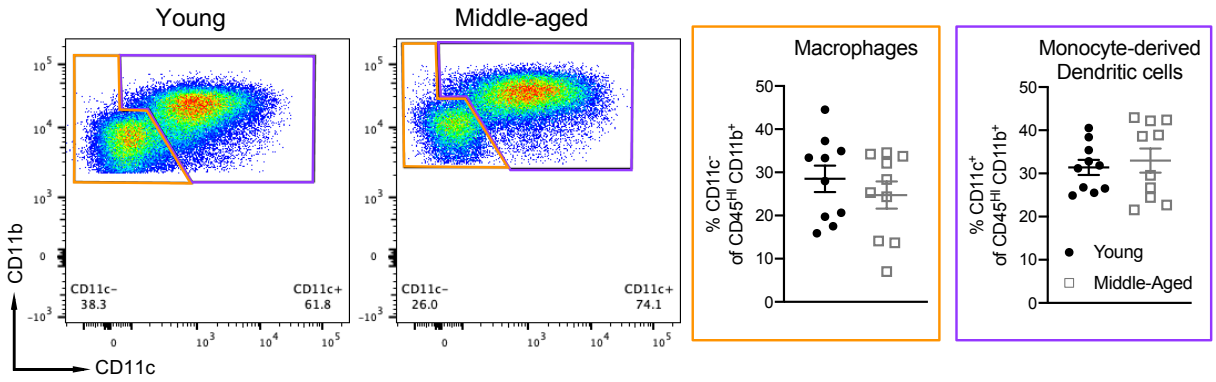

Supplementary Figure 2. The frequencies of monocyte-derived dendritic cells and macrophages in CNS infiltrates are comparable between young and middle-aged adoptive transfer recipients at peak EAE. CNS inflammatory cells were harvested from the spinal cords of young and middle-aged mice at day 10 adoptive post-transfer. Representative plots (left panels), and frequencies of macrophages ($CD45^+$ $CD11b^+$ $Ly6G^-$ $CD11c^-$) and monocyte-derived dendritic cells ($CD45^+$ $CD11b^+$ $Ly6G^-$ $CD11c^-$) of individual mice in each group. Data were obtained from n=10 mice/ group pooled from 3 independent experiments. Each symbol represents a data point generated from a single mouse. Statistical significance was determined using the unpaired 2-tailed Student's *t* test.

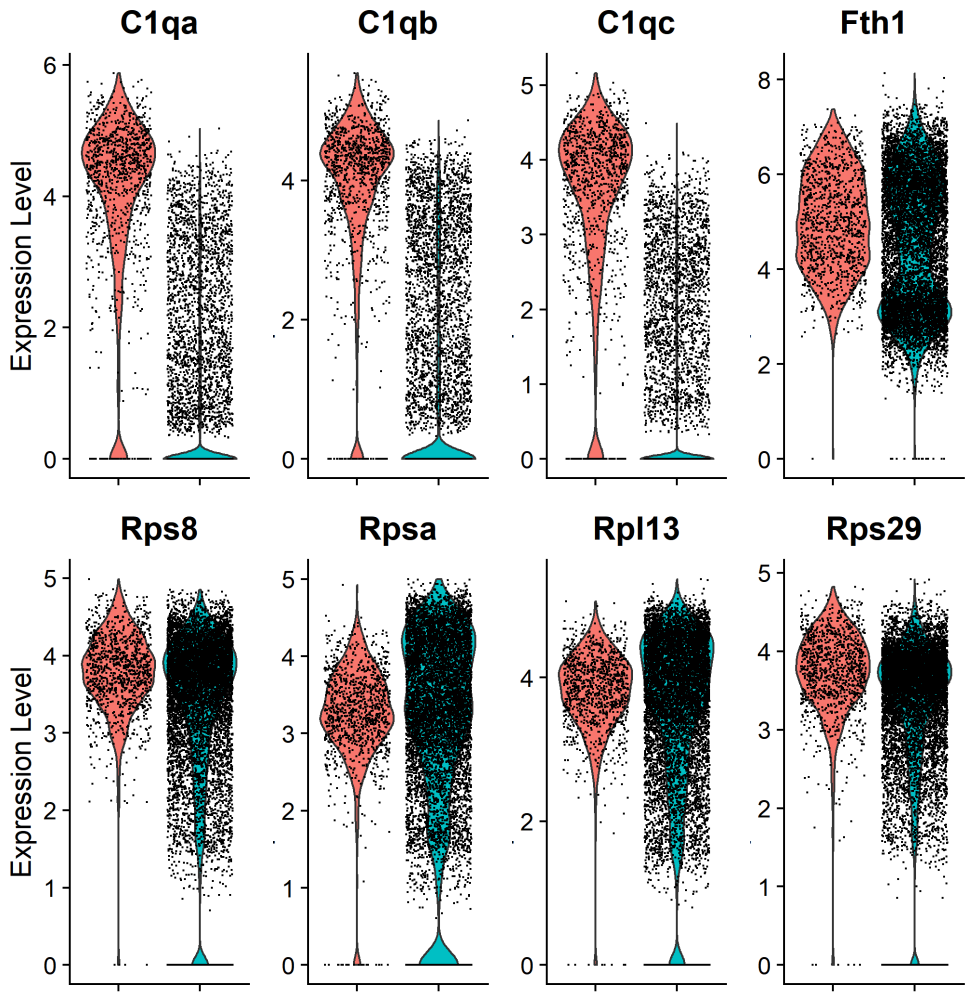

725

726 **Supplementary Figure 3. Microglia from middle-aged mice with EAE express high levels of genes**
727 **identified in microglia located in the rims of chronic active pMS lesions.** CD45^{+} mononuclear cells were
728 FACS sorted from middle-aged mice with EAE on day 10 post-cell transfer and subjected to scRNA-seq. Selected
729 differentially expressed genes in microglia (red) compared with all other cells (blue), shown as violin pots.
730 Numbers on the y-axis correspond to the z score for each gene.

731